

# 1 *In-situ* Lu – Hf geochronology of calcite

2 Alexander Simpson<sup>1,2</sup>, Stijn Glorie<sup>1,2</sup>, Martin Hand<sup>1,2</sup>, Carl Spandler<sup>1</sup>, Sarah Gilbert<sup>3</sup>, Brad Cave<sup>1</sup>

3 <sup>1</sup>Department of Earth Sciences, School of Physical Sciences, The University of Adelaide, Adelaide SA-5005, Australia

4 <sup>2</sup>Mineral Exploration Cooperative Research Centre (Minex CRC), The University of Adelaide, Adelaide SA-5005, Australia

5 <sup>3</sup>Adelaide Microscopy, The University of Adelaide, Adelaide SA-5005, Australia

6 *Correspondence to:* Alexander Simpson (alexander.simpson@adelaide.edu.au)

7 **Abstract.** The ability to constrain the age of calcite formation is of great utility to the Earth Science community, due to the  
8 ubiquity of calcite across a wide spectrum of geological systems. Here, we present the first in-situ laser ablation inductively  
9 coupled tandem [quadrapole](#) mass spectrometry (LA-ICP-MS/MS) Lu–Hf ages for calcite, demonstrating geologically  
10 meaningful ages for IOCG and skarn mineralisation, carbonatite intrusion and low grade metamorphism. The analysed samples  
11 range in age between ca. 0.9 Ga and ca. 2 Ga with uncertainties between 1.74% and 0.65% obtained from calcite with Lu  
12 concentrations as low as ca. 0.5 ppm. The Lu–Hf system in calcite appears to be able to preserve primary precipitation ages  
13 over a significant amount of geological time, although further research is required to constrain the closure temperature. The  
14 in-situ approach allows calcite to be rapidly dated while maintaining its petrogenetic context with mineralization and other  
15 associated mineral processes. Therefore, LA-ICP-MS/MS Lu–Hf dating of calcite can be used to resolve the timing of complex  
16 mineral paragenetic sequences that are a feature of many ancient rock systems. [\(Whitehouse and Russell, 1997\)](#).

Formatted: Not Highlight

Formatted: Not Highlight

Field Code Changed

## 17 **1 Introduction**

18 ~~Suspendisse~~ Calcite (CaCO<sub>3</sub>) is the main mineral phase of most carbonate sedimentary rocks and their metamorphic  
19 equivalents, [is a common diagenetic phase](#) and is a major component of carbonatites. Calcite is also a common product of  
20 hydrothermal alteration and constituent of mineralising systems where it may precipitate from fluids during pre-ore, ore-stage,  
21 and post-ore forming processes [\(Debruyne et al., 2016\)](#). The ability to directly date calcite unlocks the possibility to constrain  
22 the timing of a vast array of geological processes that can be difficult to date using conventional methods.

Formatted: Font color: Auto

Field Code Changed

23  
24 Accurate *in-situ* U–Pb geochronology of calcite has been applied to a variety of geological systems [\(e.g; Li et al., 2014; Ring  
25 and Gerdes, 2016; Roberts and Walker, 2016\)](#). However, calcite often incorporates significant quantities of Pb during  
26 crystallisation (i.e. ‘initial’ or ‘common’ Pb), which can limit the utility of U–Pb geochronology [\(Rasbury and Cole, 2009\)](#).  
27 Moreover, Pb is highly fluid mobile [\(Brugger et al., 2016\)](#), so it can be difficult to obtain primary age information with the U–  
28 Pb method in hydrothermal or strongly-altered systems [\(Roberts et al., 2020; Simpson et al., 2021b\)](#). Further, given the  
29 propensity for calcite to undergo recrystallisation, calcite U–Pb geochronology is rarely applicable to Precambrian systems as  
30 the calcite U–Pb system invariably does not remain closed over long timescales [\(Whitehouse and Russell, 1997\)](#).

Field Code Changed

Field Code Changed

Field Code Changed

Field Code Changed

Field Code Changed

32 Alternative dating systems involving the ~~radiometric-radioisotopic~~ decay of rare earth elements (REE) such as Sm–Nd and  
33 Lu–Hf, have previously been applied to calcite (e.g. Barker et al., 2009; Maas et al., 2020; Nie et al., 1999; Peng et al., 2003),  
34 based on the moderate to strong compatibility of REEs in carbonates in many systems (Debruyne et al., 2016; Elzinga et al.,  
35 2002; Terakado and Masuda, 1988; Zhong and Mucci, 1995). ~~Although it should be noted that REE compatibility will be~~  
36 ~~dependent on the conditions of calcite formation, and can vary.~~ Importantly for geochronology, experimental evidence  
37 indicates that Lu and Hf are highly immobile in many hydrothermal fluids (Brugger et al., 2016; Migdisov et al., 2016),  
38 meaning that the Lu–Hf system is ~~potentially less susceptible to resetting~~ during post-formation processes relative to the U–  
39 Pb system. However, concentrations of Lu and Hf are generally low (ppm to ppt range) in calcite, necessitating the dissolution  
40 of large quantities of material (up to 2g) per sample for conventional Lu–Hf geochronology (Maas et al., 2020). These large  
41 quantities significantly reduce the spatial resolution of the technique and have the additional problem of potential  
42 contamination from inclusions. Furthermore, age variation is difficult to detect, and bulk samples may produce meaningless  
43 ~~average age derived from mixing of age domains, mixed ages.~~ The dissolution process also removes calcite from its petrological  
44 context. The recent development of *in-situ* Lu–Hf geochronology of individual minerals by LA-ICP-MS/MS allows for rapid  
45 acquisition of spatially resolved data, ~~and has been demonstrated for garnet~~ (Ribeiro et al., 2021; Tamblyn et al., 2021) ~~and~~  
46 ~~zircon~~ (Glorie et al., 2021) (Brown et al., accepted; Glorie et al., 2021; Ribeiro et al., 2021; Simpson et al., 2021; Tamblyn et al., 2021), ~~opening new avenues for geochronology.~~  
47  
48 In this study, we present the first *in-situ* Lu–Hf dating of calcite from a variety of geological environments. We demonstrate  
49 the ~~that power of in-situ~~ calcite Lu–Hf geochronology ~~can~~ produce ~~meaningful primary~~ ages for complexly deformed and  
50 ~~hydrothermal systems, such as mineral veins, carbonate inclusions and low-grade metamorphism, that have previously been difficult to date using other geochronological~~

## 51 2 Geological Background of Samples

52 The analysed samples were selected; (1) to demonstrate that calcite Lu–Hf can date primary calcite formation in carbonatites;  
53 (2) to reveal the potential of the method to unravel complex ore systems or later events, and; (3) to characterize large calcite  
54 samples that would make suitable reference materials for *in-situ* analysis.

### 55 2.1 Phalaborwa Carbonatite, South Africa

56 The Phalaborwa Igneous Complex is located ~450 km northeast of Johannesburg, in the Limpopo Province, South Africa. The  
57 igneous complex is the result of several distinct pulses of alkaline intrusions that were emplaced into Archean granitic gneiss  
58 (Staff, 1976). The Loolekop pipe is located in the centre of the Phalaborwa Igneous Complex and was intruded by two episodes  
59 of carbonatite emplaced at the intersection of five major faults and shear zones (Basson et al., 2017; Staff, 1976). The oldest  
60 carbonatite is termed the “transgressive banded” carbonatite and has an emplacement age of  $2060.0 \pm 2.2$  Ma (baddeleyite  
61 SIMS U–Pb; Wu et al., 2011). This is intruded by a slightly younger carbonatite termed the “banded” carbonatite and has an  
62 emplacement age of  $2059.8 \pm 1.3$  Ma (baddeleyite SIMS U–Pb; Wu et al., 2011). The Phalaborwa carbonatite is unique as it is  
63 the only known example of a carbonatite containing economic Cu mineralisation (Groves and Vielreicher, 2001). In the banded

Field Code Changed

Field Code Changed

Field Code Changed

Field Code Changed

Field Code Changed

Field Code Changed

Field Code Changed

Field Code Changed

Field Code Changed

Field Code Changed

Field Code Changed

64 carbonatite-phoscorite, Cu mineralisation is primarily in the form of bornite inter-grown with valleriite with minor chalcopyrite  
65 (Staff, 1976). In the transgressive carbonatite, Cu mineralisation is present as chalcopyrite inter-grown with cubanite and  
66 valleriite (Staff, 1976). Cu mineralisation is interpreted to be magmatic-hydrothermal in origin, with Cu leached by high-  
67 temperature hydrothermal fluids at depth, precipitating along fractures within the hosting carbonatite (Le Bras et al., 2021).  
68 The sample used in this study (P01) is representative ~~offer~~ carbonatite hosted Cu-mineralisation from within the Loolekop  
69 pipe (Fig. 1). The sample is mineralogically composed of chalcopyrite inter-grown with cubanite and pyrrhotite alongside an  
70 assemblage of magnetite, dolomite, calcite, biotite, pyroxene and valleriite. As the Phalaborwa carbonatite has a well  
71 constrained crystallisation age, it provides an ideal case study to demonstrate the utility of the *in-situ* Lu–Hf method for dating  
72 igneous calcite directly associated with Cu mineralisation.

Field Code Changed

### 73 2.2 The Eastern Fold Belt, Mt Isa Block, Queensland, Australia

74 The Eastern Fold Belt of the Mount Isa Domain has experienced multiple episodes of deformation, magmatism,  
75 metamorphism, mineralisation and pervasive hydrothermal alteration across the Paleo- to Mesoproterozoic, and hence  
76 represents ~~one of~~ the most metasomatized crustal blocks on Earth (Oliver et al., 2008). Hydrothermal calcite is common across  
77 the ~~Mount Isa region, in region and is spectacularly developed in calcite pods and veins (up to 100s of metres) within~~ the Mary  
78 Kathleen Domain (Oliver et al., 1993) and in many of the IOCG deposit of the Cloncurry District. For this study we have  
79 selected calcite samples from the Lime Creek calcite quarry and the Mt Elliott IOCG deposit for Lu–Hf analysis. ~~The Mt Isa~~  
80 ~~Domain has both regional and deposit level age constraints, making it a good area to demonstrate the technique~~ ~~These sample~~  
81 ~~locations have good constraints on expected mineralisation ages, making them suitable samples to demonstrate the technique.~~  
82

Field Code Changed

83 The Lime Creek quarry is one of ~~a~~ number of large calcite pods or veins that are exposed in Mary Kathleen Domain. The Lime  
84 Creek quarry is hosted within the ca. 1760 Ma Argylla Formation and lies along the steeply dipping NNW-trending Tribulation-  
85 Lime Creek Fault, which offsets regional-scale ‘D<sub>2</sub>’ folds (Marshall, 2003). Breccias along this fault contain clasts of calc-  
86 silicate rocks and metadiorite ~~clasts~~ with a matrix consisting of albite-actinolite-diopside-biotite-titanite-apatite that are  
87 subsequently overprinted by the undeformed Lime Creek calcite-dominated veins (Marshall, 2003). These veins are extremely  
88 coarse-grained with calcite crystals larger than 1 m<sup>3</sup>, actinolite crystals over 1 m in length, and apatite, biotite, diopside and  
89 titanite grains over 20 cm in diameter (Marshall, 2003; Oliver et al., 1993). Based on cross-cutting relationships, it is interpreted  
90 that the Lime Creek vein system, and other calcite pods/veins of this style precipitated post-faulting during late-‘D<sub>3</sub>’  
91 deformation (ca. 1550–1500 Ma) of the Isan Orogeny (Giles and Nutman, 2002; Marshall, 2003). This style of veining is  
92 common throughout the Mary Kathleen Domain and provides evidence of km-scale fluid transport during late-stage  
93 metamorphism (Oliver et al., 1993). Based on C and O isotope analysis of calcite from these veins, they are interpreted to have  
94 formed from hydrothermal fluids likely associated with the intrusion of the ca. 1530 to 1500 Ma Williams-Naraku Batholiths  
95 (Oliver et al., 1993). Although no direct dating has been completed on the Lime Creek Quarry, titanite from the nearby and  
96 cognate Knobby Quarry have produced three titanite U–Pb ages of 1521 ± 5 Ma, 1527 ± 7 Ma, and 1555 ± 5 Ma (Oliver et al.,

Field Code Changed

Field Code Changed

Field Code Changed

Field Code Changed

97 2004). The sample analysed in this study (LC1) consists of very coarse-grained calcite with coarse-grained diopside collected  
98 from a large calcite pod in the Lime Creek Quarry (Fig. 1).

99

100 Mt Elliott is an IOCG deposit located in the Eastern Fold Belt of the Mount Isa Inlier (Duncan et al., 2011). The deposit is  
101 situated within northwest striking splays of the Mount Dore Fault (Duncan et al., 2011; Wang and Williams, 2001), and is  
102 hosted within skarn-altered and deformed phyllites and schists (Garrett, 1992; Wang and Williams, 2001). The host rocks were  
103 metamorphosed to lower amphibolite facies during the ca. 1600-1580 Ma 'D<sub>2</sub>' deformation of the Isan Orogeny (Garrett, 1992;  
104 Wang and Williams, 2001). The formation of early albite-hematite (red rock) alteration enhanced brittle fracturing and  
105 brecciation of the shale (Garrett, 1992). This was infilled by two stages of open-space skarn development: (1) diopside-  
106 magnetite-hematite-calcite-titanite-allanite-phlogopite, and: (2) actinolite-scapolite-magnetite-andradite-calcite-epidote-  
107 allanite-chlorite and biotite (Garrett, 1992; Wang and Williams, 2001). Sulphides in the second stage include chalcopyrite,  
108 pyrrhotite and pyrite (Garrett, 1992). Although the two skarn assemblages are difficult to distinguish mineralogically, the  
109 second episode is the most widespread and represents the major Cu-Au event (Garrett, 1992; Wang and Williams, 2001). A  
110 variety of geochronological techniques have been applied to constrain the age of Cu-Au mineralisation. The earliest phase of  
111 skarn development has been dated at 1530 ± 11 Ma (U-Pb titanite; Duncan et al., 2011). The second stage of skarn development  
112 associated with Cu-Au mineralisation has been dated at 1513 ± 5 Ma (molybdenite Re-Os; Duncan et al., 2011) and 1510 ±  
113 3 Ma (actinolite Ar-Ar; Wang and Williams, 2001). Two outcrop samples from the Mount Elliot Cu-Au deposit were selected  
114 for Lu-Hf geochronology. Mt Elliott 1 (ME 1) consists of coarse-grained pink-coloured calcite that is coeval with the formation  
115 of diopside, scapolite and magnetite (Fig. 1). Although the paragenesis of this sample is relatively unconstrained, the lack of  
116 sulphides may indicate that this sample belongs to the early pre-mineralisation skarn assemblage. Calcite from sample Mt  
117 Elliott 2 (ME 2) is coeval with the formation of andradite, pyrite, chalcopyrite, pyrrhotite and magnetite (Fig. 1). The close  
118 relationship between calcite and chalcopyrite in this sample indicates that it is associated with the main Cu-Au bearing skarn  
119 assemblage.

### 120 2.3 Flin Flon Volcanic Massive Sulphide (VMS) Deposit, Canada

121 The Flin Flon Greenstone Belt stretches across central Manitoba through to east central Saskatchewan and hosts several world-  
122 class Zn-Cu VMS deposits including the Flin Flon, Callinan and 777 deposits (Koo and Mossman, 1975). Zn-Cu  
123 mineralisation is interpreted to have formed contemporaneously with deposition of the 1888.9 ± 1.6 Ma Millrock member  
124 during the Trans-Hudson Orogeny (Gibson et al., 2012; Koo and Mossman, 1975; Rayner, 2010). The Flin Flon Zn-Cu orebody  
125 is recognised to have undergone six distinct deformation events that have affected the shape of the deposit (Lafrance et al.,  
126 2016; Schetselaar et al., 2017). 'D<sub>1</sub>' and 'D<sub>2</sub>' were associated with the intra-oceanic accretion of the Flin Flon Arc to other  
127 volcanic terrains before ca. 1872 Ma (Lafrance et al., 2016). 'D<sub>3</sub>' occurred from 1847-1842 Ma as a response to the final  
128 accretion of the Flin Flon Terrane to the Glennie Terrane, producing west-verging folds within stacked, east dipping thrust  
129 sheets of basement and cover rocks bounded by NNW-striking thrust faults (Lafrance et al., 2016). 'D<sub>4</sub>' resulted from the

Field Code Changed

Field Code Changed

Field Code Changed

Field Code Changed

Field Code Changed

Field Code Changed

Field Code Changed

130 collision between the Flin Flon and Glennie complex with the Sask Craton and is broadly coeval with the ca. 1840 Ma Phantom  
131 Lakes dyke (Gibson et al., 2012; Lafrance et al., 2016). 'D<sub>5</sub>' deformation produced a penetrative regional cleavage (S<sub>5</sub>) that is  
132 defined by a continuous chloritic foliation ubiquitous in the volcanic basement rocks (Gibson et al., 2012; Lafrance et al.,  
133 2016). EWE–WNW directed compression during 'D<sub>6</sub>' deformation produced a second regional penetrative cleavage and  
134 reactivated a variety of regional-scale faults (Gibson et al., 2012; Lafrance et al., 2016). Regional greenschist to granulite facies  
135 metamorphism is associated with D<sub>5-6</sub> deformation at ca. 1820–1790 Ma (Schneider et al., 2007). The Flin Flon mine horizon  
136 was imbricated during 'D<sub>3</sub>' thrusting with the shape of the ore lenses moulded during 'D<sub>4</sub>' and 'D<sub>5</sub>' deformation (Schetselaar  
137 et al., 2018). Regional greenschist to amphibolite grade metamorphism occurred between 1820 – 1790 Ma (U-Pb monazite;  
138 Schneider et al., 2007), with rocks in the Flin Flon deposit reaching greenschist facies (Koo and Mossman, 1975). The sample  
139 selected for this study is from the hydrothermally altered and sheared footwall of the Flin Flon VMS deposit. This sample is  
140 composed of highly foliated chlorite and calcite with disseminated pyrite and residual titanomagnetite. A band of highly  
141 foliated calcite was selected for Lu–Hf analysis (sample FF014; Fig. 1) to constrain the age of syn-metamorphic shearing of  
142 the deposit.

### 143 2.3 Yates U-Th prospect, Otter Lake Area, Grenville Province, Canada

144 The Otter Lake area is located in SE Ontario within the Grenville Province. The Grenville Province can be distinguished from  
145 surrounding provinces based on various structural, metamorphic and isotopic signatures attributed to the overprinting ca. 1080–  
146 985 Ma Grenvillian Orogeny (Rivers, 2015). This orogenic event produced widespread metamorphism from granulite to  
147 amphibolite facies ~~between ca. 1090–990 Ma~~ (Breemen and Corriveau, 2005), accompanied by widespread hydrothermal alteration in the Otter Lake area  
148 (Kretz et al., 1999). The Yates U-Th prospect is located approximately 100 km northwest of Ottawa, and is renowned for the  
149 occurrence of pegmatites that contain large euhedral crystals of apatite set within a matrix of predominantly orange-pink  
150 calcite, with diopside, allanite, titanite, fluorite, thorite and phlogopite (Schumann et al., 2019). A wide range of dates have  
151 been produced from the Yates mine; including titanite Pb–Pb and U–Pb ages between ca. 1020 and 998 Ma (Frei et al., 1997;  
152 Kennedy et al., 2011); apatite Pb–Pb, and U–Pb ages of 913 ± 7 Ma (Barfod et al., 2005), 933 ± 12 Ma and 920 – 850 Ma  
153 (Chew et al., 2011; Xiang et al., 2021) respectively, and an apatite Lu–Hf age of 1031 ± 6 Ma (Barfod et al., 2005). In addition,  
154 Simpson et al. (2021a) obtained an *in-situ* Lu-Hf apatite age of 1000 ± 11 Ma (when corrected for laser induced elemental  
155 fractionation). Importantly, the apatite Lu–Hf and Pb–Pb ages have been obtained from the same large apatite crystal,  
156 indicating that the Lu–Hf and U–Pb systems have been decoupled (as opposed to multiple generations of apatite growth).  
157 Barfod et al. (2005) argued that late-stage fluid interactions may have affected Pb retentivity in the apatite, as the apatite was  
158 unlikely to be above the apatite Pb closure temperature at ca. 913 Ma. Calcite from a specimen containing coarse-grained  
159 euhedral apatite with pink calcite, quartz and diopside was selected for calcite Lu–Hf analysis (OL-MB, Fig. 1). The apatite is  
160 enclosed in the sampled calcite, and is interpreted to have crystallised just prior to the calcite, but during the same hydrothermal  
161 event.

Field Code Changed

Field Code Changed

Field Code Changed

Field Code Changed

Field Code Changed

Field Code Changed

Field Code Changed

Field Code Changed

Field Code Changed

Field Code Changed

Field Code Changed

Field Code Changed

### 162 3 Method

163 The samples were mounted in 2.5 cm diameter epoxy mounts and screened for Lu concentration by LA-ICP-MS to determine  
164 suitability for Lu–Hf analysis ([Supplementary File 2](#)). Mineral liberation analysis (MLA) maps were obtained using a Hitachi  
165 SU3800 scanning electron microscope (SEM) to reveal the petrogenetic context of the analysed calcite.

#### 166 3.1 In-Situ Lu-Hf Dating Method

167 Analysis was conducted at Adelaide Microscopy, The University of Adelaide. Calcite samples were analysed using a  
168 RESOLUTION 193 nm laser ablation system (Applied Spectra) with a S155 sample chamber (Laurin Technic). The laser ablation  
169 system was coupled to an Agilent 8900 tandem mass spectrometer (ICP-MS/MS). The methodology largely follows that of  
170 Simpson et al. (2021a) including an initial instrument tune conducted with no NH<sub>3</sub> in the reaction cell to achieve robust plasma  
171 conditions (U/Th = 1.00-1.05) and minimal oxide interferences (ThO/Th <0.2%). A carrier gas of 3.5 mL/min N<sub>2</sub> was added  
172 after the sample cell in order to increase sensitivity (Hu et al., 2008). Analytical conditions are included in [Supplementary appendix Table 1](#).

173  
174 Methods for separation of <sup>176</sup>Hf from <sup>176</sup>Lu and <sup>176</sup>Yb follow that of Simpson et al. (2021a). In more detail, the Agilent 8900x  
175 utilises a reaction cell between two quadrupole mass analysers, which can be used to separate isobaric interferences. The first  
176 quadrupole is used as a mass filter (e.g., when set to mass 176, only <sup>176</sup>Lu, <sup>176</sup>Yb, and <sup>176</sup>Hf can pass), thereby minimizing  
177 potential background interferences and other, unwanted reactions. Following this, a mixture of 10% NH<sub>3</sub> and 90% He is added  
178 to the reaction cell (at a rate of 3 mL/min). This mixture is optimized to promote formation of the Hf reaction product  
179 Hf((NH)(NH<sub>2</sub>)(NH<sub>3</sub>)<sub>3</sub>)<sup>+</sup> and the second quadrupole is set to 82 amu higher than the first (e.g., Q1 = 176 amu and Q2 = 258  
180 amu). This method minimizes the equivalent Lu and Yb reaction products ([~0.03% for Lu, and below detection for Yb](#)), such  
181 that the isobaric interferences on <sup>176</sup>Hf are negligible (Simpson et al., 2021a). Lens voltages were tuned to increase sensitivity  
182 on the Hf reaction product (Simpson et al., 2021a). In order to calculate Lu/Hf ratios, <sup>176</sup>Hf (+82) was measured directly, <sup>175</sup>Lu  
183 was measured as a proxy for <sup>176</sup>Lu, and <sup>178</sup>Hf (+82) measured as a proxy for <sup>177</sup>Hf, [with present day isotopic abundances used  
184 to convert isotopes](#) (Simpson et al., 2021a). [<sup>176</sup>Hf/<sup>176</sup>Lu, <sup>176</sup>Lu/<sup>177</sup>Hf, and <sup>176</sup>Hf/<sup>177</sup>Hf ratios were calculated as part of the normalization to NIST610,  
185 as opposed to separately converting measured <sup>175</sup>Lu and <sup>178</sup>Hf into <sup>176</sup>Lu and <sup>178</sup>Hf. In more detail, if we assume that the  
186 <sup>176</sup>Lu/<sup>175</sup>Lu ratio \(or <sup>177</sup>Hf/<sup>178</sup>Hf ratio\) is identical between NIST SRM 610 and all analysed samples, a correction factor  
187 calculated from the % difference between the <sup>175</sup>Lu/<sup>178</sup>Hf ratio measured in NIST SRM 610 and the published <sup>176</sup>Lu/<sup>177</sup>Hf will  
188 correct the unknowns for matrix independent fractionation and differences in isotopic abundance. <sup>43</sup>Ca was measured for  
189 internal normalization of trace element abundances, and the following isotopes were measured to monitor for inclusions: <sup>27</sup>Al,  
190 <sup>47</sup>Ti, <sup>89</sup>Y, <sup>90</sup>Zr, <sup>140</sup>Ce, and <sup>172</sup>Yb.](#)

191  
192 Lutetium abundances in most calcite samples are low (< 6 ppm), so we employed a large laser diameter of 257 μm, and a  
193 repetition rate of 10 Hz to maximize sensitivity. [High sensitivity is important in order to either measure common Hf \(in this](#)

Field Code Changed

Field Code Changed

Field Code Changed

194 case <sup>178</sup>Hf), or demonstrate that <sup>176</sup>Hf is sufficiently above detection limits that the effects of common Hf are negligible. Smaller  
195 spot sizes could be employed for higher Lu and/or higher Hf samples. An extra 20 seconds delay was added after each interval  
196 of sample ablation in order to ensure the washout had reached background levels. NIST SRM 610 glass (<sup>176</sup>Lu/<sup>177</sup>Hf: 0.1379  
197 ± 0.005, <sup>176</sup>Hf/<sup>177</sup>Hf: 0.282122 ± 0.000009; Nebel et al., 2009) was used as the primary reference material and was analyzed  
198 using a spot size of 43 μm. The smaller spot size was required to ensure that <sup>175</sup>Lu was measured in pulse counting mode (<4  
199 Mcps). Consistent with observations in Simpson et al. (2021a), Lu and Hf showed no measureable down-hole fractionation in  
200 the analysed carbonates (fig. 2), as such, no down-hole correction was applied to the data. demonstrated that there is no  
201 downhole fractionation in Lu-Hf isotope ratios, therefore spot sizes do not need to be matched between standards and  
202 unknowns.

203  
204 A side effect of the use of large ablation spots is ‘plasma loading’ for which the introduction of a large amount of material  
205 reduces the ionizing efficiency of the plasma (Kroslakova and Günther, 2007). Plasma loading was observed in the time  
206 resolved signals, with a reduction in signal intensity for all isotopes after ~10 to 15 seconds of ablation. Following this, the  
207 signal stabilized after ~18 seconds of ablation (Fig. 2). Importantly, this variation in signal intensity was not observed in the  
208 calculated time resolved isotope ratios (Fig. 2), which means that identical ratios were calculated whether this decrease in  
209 signal intensity was included or not in the ratio calculation. Importantly, plasma loading can be affected by sample matrix  
210 (Kroslakova and Günther, 2007), especially for minerals containing easily ionized elements such as Ca. This necessitates  
211 matrix matched calibration, despite the observed lack of down-hole changes in Lu–Hf ratios (Simpson et al., 2021a).

212  
213 The large ablation volume caused accumulation of ablated material in the tubing and on the interface cones during the first  
214 analytical session, which coincided with a decrease in signal intensity over time. Consequently, session 1 records slightly more  
215 signal drift compared to session 2. However, there was no measureable corresponding drift observed in the calculated isotopic  
216 ratios, apart from a slight decrease in precision due to the lower sensitivity toward the end of the run. Therefore, we recommend  
217 that cones are cleaned prior to analysis, and suggest a maximum session duration of approximately 7 hours when using spot  
218 diameters of >200 μm. In addition to this, the accumulated material was sometimes mobilized in later analyses, potentially  
219 contaminating data. This was observed by increases in Al during the start of ablation that decayed down to background levels.  
220 Importantly, similar Al spikes were not observed during background measurement, indicating contamination due to material  
221 remobilized during ablation is likely, hence why the additional 20 seconds of washout did not fix this. This contamination did  
222 not generally produce a measurable effect on calculated Lu/Hf ratios. However, we stress that this contamination is important  
223 to monitor as Hf concentrations are sometimes in the ppt level. As such we recommend close monitoring of signals, particularly  
224 Al concentrations, and the removal of 1-3 seconds of each analysis after signal stabilisation if necessary.

225  
226 3.2 Data Processing

Formatted: Superscript

Field Code Changed

Formatted: Superscript

Field Code Changed

Field Code Changed

227 ~~Analysis of the matrix was done using the LACPM Standardization procedure for LACPM and LACPM-MS analysis. The initial common Hf was used for~~  
228 ~~internal normalization of trace element concentrations.~~ Although the high Ca cps for all analysed samples indicate that they  
229 are close to stoichiometric calcite, there may be slight inaccuracies in calculated element concentrations due to major element  
230 substitutions from Mg, Fe, and Mn that are common in carbonates. However, element concentrations were largely used as  
231 relative proxies to monitor for inclusions.

232  
233 Background subtractions, element concentrations and ratio calculations were performed using LADR software (Norris and  
234 Danyushevsky, 2018). Where  $^{178}\text{Hf}$  was measured above detection limits ( $\sim 2$  ppt for  $^{178}\text{Hf}$ ), common Hf corrections were  
235 applied to the data after background subtractions, but prior to normalization to the standard. In more detail, the  $^{178}\text{Hf}$  cps  
236 measurement for each sampling cycle of the analysis period of each laser spot was used to calculate the common Hf component  
237 of the corresponding  $^{176}\text{Hf}$  cps measurement, using the following equation:

$$i^{176}\text{Hf}_r = i^{176}\text{Hf}_m - \left( \frac{i^{176}\text{Hf}}{i^{178}\text{Hf}} \right) c \times i^{178}\text{Hf}_m$$

239 Where  $^{176}\text{Hf}_r$  = radiogenic  $^{176}\text{Hf}$ ,  $^{176}\text{Hf}_m$  = measured  $^{176}\text{Hf}$ ,  $^{178}\text{Hf}_m$  = the measured  $^{178}\text{Hf}$  and  $\left( \frac{i^{176}\text{Hf}}{i^{178}\text{Hf}} \right) c$  = the initial or 'common'  
240  $^{176}\text{Hf}/^{178}\text{Hf}$  ratio. These corrections were applied using an assumed initial  $^{176}\text{Hf}/^{178}\text{Hf}$  ratio of  $0.192 \pm 0.004$ , which is equivalent  
241 to a  $^{176}\text{Hf}/^{177}\text{Hf}$  ratio of  $0.2816 \pm 0.006$ . This value is based on the Hf evolution of the crust, with uncertainty that comfortably  
242 covers likely natural variation. The uncertainty on the initial  $^{176}\text{Hf}/^{178}\text{Hf}$  ratio used for the common Hf corrections has been  
243 propagated to the final ages, in order to account for any inaccuracies introduced by value used. However, as most analyses  
244 have  $<1\%$  common Hf (Table 1), any inaccuracy related to the initial  $^{176}\text{Hf}/^{178}\text{Hf}$  ratio is negligible compared to the total  
245 uncertainty estimates given Hf isotopes do not vary significantly with time (Fisher and Vervoort, 2018; Vervoort, 2014). (Spencer et al., 2020) Such  
246 corrections, however, should be used with caution for samples with higher common Hf, although the dataset presented in this  
247 ~~work is not intended to be used for this purpose. (Spencer et al., 2020) High common Hf is not a problem for this dataset.~~

248  
249 Subsequent to this correction, isotopic ratios were corrected using an external reference material bracketing approach  
250 (commonly used in LA-ICP-MS geochronology), with primary and secondary reference materials interspaced with unknowns  
251 through each analytical session. The data was normalized to NIST SRM 610 glass to correct for drift and matrix independent  
252 fractionation. The Lu–Hf isotopic ratios published in Nebel et al. (2009) were used for the NIST610 SRM normalisation.  
253 Following this,  $^{176}\text{Hf}/^{176}\text{Lu}$ ,  $^{176}\text{Lu}/^{177}\text{Hf}$ , and  $^{176}\text{Lu}/^{176}\text{Hf}$  ratios were corrected to MKED calcite. Although the age of MKED  
254 calcite is currently not independently constrained, calcite is interpreted from textural evidence to have formed with the MKED  
255 titanite reference material, and therefore the titanite TIMS U–Pb age was used ( $1517.32 \pm 0.32$  Ma; Spandler et al., 2016).  
256 Further details are outlined in appendix A were corrected to MKED calcite, although the age of this sample is currently not  
257 independently constrained, it is interpreted to have formed with the MKED titanite reference material, and therefore the titanite  
258 TIMS U–Pb age was used ( $1517.32 \pm 0.32$  Ma; Spandler et al., 2016). Further details are outlined in appendix A. This ratio is not used in this study (Ruest et al., 2017) for U–Pb data based on U–Pb

Field Code Changed

Formatted: Font color: Auto

Formatted: Font color: Auto

Formatted: Font color: Auto

Formatted: Font color: Auto

Formatted: Font color: Auto

Field Code Changed

Field Code Changed

Field Code Changed



259 between the measured and expected Lu–Hf ratio in the standard is applied (as a % correction factor) to the ratios of the  
260 unknowns. This offset is inferred to be due to a combination of laser induced (matrix-dependent) elemental fractionation and  
261 plasma loading. The uncorrected ages for MKED calcite as well as for ME 1 across four analytical sessions are constant within  
262 uncertainty, indicating the age offset is a systematic analytical bias that is applicable to the calcite samples of unknown age  
263 (Sup-Fig. A23). Weighted average ages were calculated using ISOPLOT (Vermeesch, 2018), using the  $^{176}\text{Lu}$  decay constant  
264 determined by Söderlund et al. (2004);  $0.00001867 \pm 0.00000008 \text{ Myr}^{-1}$

Field Code Changed

Field Code Changed

265  
266 Correct handling of uncertainties in geochronology is important in order to draw accurate conclusions about the resulting ages.  
267 As per the recommendations for LA-ICP-MS U-Pb uncertainty propagation in Horstwood et al. (2016), uncertainties are  
268 categorised as random, in which case they are propagated to individual analyses, or systematic, in which case they are  
269 propagated to the final calculated age. As such, the uncertainties associated with the measurement of the primary standard  
270 (NIST SRM 610) have been propagated to the uncertainties of individual analyses. The following systematic uncertainties  
271 have been propagated to the final ages: Measurement uncertainty on the secondary standard (MKED C), uncertainty on the  
272 titanite U-Pb age used as the reference age for MKED C, uncertainties associated with the  $^{176}\text{Lu}$  decay constant, the reference  
273  $^{176}\text{Hf}/^{177}\text{Hf}$  ratios for NIST SRM 610. Although for completeness it would be good to propagate uncertainty relating to potential  
274 differences in  $^{175}\text{Lu}/^{176}\text{Lu}$  and  $^{177}\text{Hf}/^{178}\text{Hf}$  between NIST SRM 610 and samples (i.e. natural variation in these ratios), currently  
275 there appears to be no data on this. These uncertainties are likely to be negligibly small relative to the overall uncertainty  
276 estimates for the analyses. (Vervoort et al., 2004) The uncertainty associated with the reference  $^{176}\text{Lu}/^{177}\text{Hf}$ ,  $^{176}\text{Lu}/^{176}\text{Hf}$ , and  $^{176}\text{Hf}/^{176}\text{Lu}$  ratios of NIST  
277 SRM 610 are not propagated, as the correction factor associated with NIST610 SRM is cancelled during the correction to  
278 MKED calcite (as the NIST610 SRM correction factor is applied equally to MKED calcite and the unknowns samples, and  
279 thus becomes redundant). Uncertainty relating to long term reproducibility of the standards has not been propagated, as the  
280 standard data for all sessions does not show scatter outside of what would be expected from a single population. More data,  
281 however, is required to fully constrain this.

#### 282 4 Lu-Hf Results

283 The analysed calcite generally contain < 1% common Hf, apart from sample P01, which contains up to 13% common Hf in  
284 individual analyses (Table 1). Consequently, the common Hf corrections are small (or effectively non-existent), and the  
285 resultant ages are not significantly affected by the assumed initial  $^{176}\text{Hf}/^{177}\text{Hf}$  ratio. Corrected and uncorrected data are included  
286 in Supplementary File 1. The inverse isochron and weighted mean single-spot Lu–Hf ages, reported below, are corrected  
287 against MKED calcite for matrix-dependant fractionation and common-Hf corrected (where relevant) (Fig. 3). For analyses  
288 with inclusions, the signals have been cropped to remove inclusions or, in the case of more significant signal disturbances,  
289 excluded from age calculations. Inclusions were detected in the following samples: MKED calcite (6), LC1 (1), P01 (19) and  
290 FF014 (6). Excluded data points are included in supplementary file 1. Due to the large number of inclusions, P01 was analysed

291 ~~over two sessions. Data is presented as inverse isochrons (Li and Vermeesch, 2021), and as common Hf corrected weighted~~  
292 ~~average ages (Fig. 3).~~

Field Code Changed

## 293 5 Discussion

294 The Phalaborwa carbonatite sample produced a ~~hf corrected weighted average Lu-Hf age of  $20504 \pm$~~   
295  ~~$340$  Ma (Fig. 3), consistent with previous baddeleyite U–Pb SIMS ages ( $\sim 2060$  Ma; Wu et al., 2011). Importantly, the~~  
296 ~~consistency between the calcite Lu–Hf age and existing constraints on carbonatite formation demonstrates that calcite Lu–Hf~~  
297 ~~dating can produce primary age information for early Paleoproterozoic calcite. This result also demonstrates that calcite Lu–~~  
298 ~~Hf geochronology is a viable technique to directly date carbonatite magmatism and associated mineralisation, even in the case~~  
299 ~~of old calcite samples with only  $\sim 0.5$  ppm Lu.~~

Field Code Changed

301 The ~~calcite-weighted average~~ Lu–Hf ages for samples ME 1 and ME 2 are  ~~$153840 \pm 9$  Ma and  $15040 \pm 123$  Ma, respectively~~  
302 (Fig. 3). The ages of these samples are consistent with the paragenetic timing of alteration at Mt Elliott, providing evidence  
303 for calcite precipitation during at least two temporally distinct alteration events. Sample ME 1 is from a coarse calcite-diopside-  
304 scapolite-magnetite vein that does not contain sulfides (Fig. 1), the age is, therefore, consistent with formation prior to the  
305 major  $\sim 1510$  Ma Cu–Au mineralisation event (Duncan et al., 2011; Wang and Williams, 2001). In addition, this age overlaps  
306 with a titanite U–Pb age from the Mt Elliott deposit ( $1530 \pm 11$  Ma; Duncan et al., 2011), and is potentially related to regional  
307 Na–Ca alteration between ca. 1555 and ca. 1521 Ma (Oliver et al., 2004). The  ~~$15040 \pm 123$  Ma~~ age obtained from sample ME 2  
308 that has an ore stage paragenesis conforms with the  $^{207}\text{Pb}/^{206}\text{Pb}$  age of cogenetic andradite ( $1507 \pm 35$  Ma; ~~Sup. Fig. 3 appendix B~~), and  
309 overlaps with the ca. 1510 Ma main mineralisation event (Duncan et al., 2011; Wang and Williams, 2001). ~~Additionally, data~~  
310 ~~for ME1 was pooled from all four analytical sessions in order to test reproducibility. Similar to the standard (MKED1; appendix~~  
311 ~~A) ~~the data were corrected for instrumental mass bias using the  $^{176}\text{Yb}/^{174}\text{Yb}$  ratio and the  $^{176}\text{Lu}/^{175}\text{Lu}$  ratio. The  $^{176}\text{Lu}/^{175}\text{Lu}$  ratio was determined using the  $^{176}\text{Lu}/^{175}\text{Lu}$  ratio of the standard (MKED1; appendix~~  
312 ~~A) and the  $^{176}\text{Lu}/^{175}\text{Lu}$  ratio of the sample. The  $^{176}\text{Lu}/^{175}\text{Lu}$  ratio of the sample was determined using the  $^{176}\text{Lu}/^{175}\text{Lu}$  ratio of the standard (MKED1; appendix~~~~

Field Code Changed

Field Code Changed

Field Code Changed

Field Code Changed

313 Sample LC1, from the Lime Creek quarry, Eastern Fold Belt, Mt Isa Inlier produced an age of  $1513 \pm 256$  Ma, consistent with  
314 published titanite U–Pb ages ( $1521 \pm 5$  Ma  $1527 \pm 7$  Ma) from the nearby Knobby Quarry (Oliver et al., 2004). Additionally,  
315 this age is consistent with the intrusion of the ca. 1530–1500 Ma Williams–Naraku batholiths, which is interpreted to be the  
316 source of the fluids from which the calcite precipitated (Oliver et al., 1993; Page and Sun, 1998). Our results for this sample  
317 further demonstrate that calcite Lu–Hf geochronology is an effective technique for constraining the age of calcite  
318 mineralisation.

Field Code Changed

Field Code Changed

319  
320 Sample OL–MB from Otter Lake produced a Lu–Hf age of  $892 \pm 12$  Ma (Fig. 3). This age is significantly younger than the  
321 apatite solution Lu–Hf age of  $1030 \pm 6$  Ma (Barfod et al. (2005) and the *in-situ* apatite Lu–Hf age of  $1000 \pm 11$  Ma (Simpson  
322 et al. 2021), but is similar to the apatite Pb–Pb age of  $913 \pm 7$  Ma (Barfod et al. 2005) and the latest stage of extensional activity  
323 on the nearby Bancroft Shear Zone ( $1045 - 893$  Ma, Ar–Ar phlogopite; Cosca et al., 1995). Given the similarity between the

Field Code Changed

Field Code Changed

324 ca. 0.9 Ga ages, obtained by different methods, it seems likely that the calcite either grew or records Lu–Hf isotopic resetting  
325 during the same event that induced resetting of the apatite Pb–Pb system. The slight difference between the calcite Lu–Hf age  
326 ( $894 \pm 12$  Ma) and apatite Pb–Pb age ( $913 \pm 7$  Ma) may be due to analytical (i.e. mixing of age domains in the solution Pb–Pb  
327 age) rather than geological reasons, particularly given an individual crystal of apatite from the Yates mine produced a U–Pb  
328 age range of 920–850 Ma (Xiang et al., 2021). ~~The age difference may also be due to underestimation of uncertainties.~~ Large  
329 (~3cm) apatite crystals such as the one analysed by Barfod et al. (2005) are expected to have Pb closure temperatures of up to  
330 600 °C (Barfod et al., 2005; Krogstad and Walker, 1994), giving a possible upper limit to Lu–Hf closure in calcite. We note  
331 that this is significantly higher than the closure temperature of Ar–Ar in phlogopite (ca. 400 °C), indicating that the Otter Lake  
332 area potentially had a different thermal history and/or that isotopic resetting in the apatite and calcite was aided by late fluid  
333 interactions, as hypothesised by Barfod et al., (2005). As such, further work is required to constrain the Lu–Hf closure  
334 temperature in calcite.

335

336 The *in-situ* Lu–Hf age of  $181007 \pm 198$  Ma for the cleavage-hosted calcite vein from the Flin Flon VMS deposit (FF14; Fig.  
337 3), as expected, is younger than the timing of initial mineralisation at the deposit (Koo and Mossman, 1975; Rayner, 2010;  
338 Stern et al., 1995). Instead, the age is in excellent agreement with ca. 1820–1790 Ma regional peak greenschist to amphibolite  
339 grade metamorphism (Schneider et al., 2007), suggesting the calcite precipitated during metamorphism related to deformation  
340 stage ‘D<sub>5</sub>’ or ‘D<sub>6</sub>’, associated with the final collision between the Flin Flon–Glennie Complex and the Sask Craton (Lafrance  
341 et al., 2016). This regional event locally reached maximum greenschist-facies metamorphism (Koo and Mossman, 1975),  
342 suggesting the calcite grew under low-grade metamorphic conditions. Sample FF014, therefore, demonstrates that calcite Lu–  
343 Hf geochronology has the potential to date low grade metamorphism, which has been difficult using traditional dating methods  
344 (e.g. Henrichs et al., 2018).

345

346 In summary, we demonstrate that *in-situ* Lu–Hf geochronology can produce ~~both accurate and precise~~ geologically meaningful  
347 ~~(0.5–1.7% uncertainty)~~ ages for calcite from a variety of mineralisation styles (e.g. IOCG, carbonatite, and skarn alteration) as  
348 well as greenschist-facies metamorphism. The technique also has great potential to date a range of other geological settings  
349 and processes (e.g., chemical sedimentation, carbonation reactions) provided calcite contains sufficient Lu for analysis.

## 350 5.1 Limitations

351 The success rate of the *in-situ* Lu–Hf dating approach in calcite is intrinsically related to; (1) the concentration of Lu, and; (2)  
352 the ingrowth time for radiogenic Hf (Fig. 4). Generally, the method is more suitable for REE-rich calcite typically observed in  
353 mineral deposits and carbonatites, and/or for Precambrian samples. In addition, the currently available mass-spectrometers  
354 require large laser beam diameters (257 μm) for successful calcite Lu–Hf dating, limiting spatial resolution compared to most  
355 laser-ablation dating techniques. We note that for high Lu samples, such as ME 1 (or samples that incorporate common Hf),  
356 smaller spot sizes are feasible. Additionally-However, particularly in hydrothermal settings, calcite often forms large, mm to

Field Code Changed

Field Code Changed

Field Code Changed

Field Code Changed

Field Code Changed

Field Code Changed

Field Code Changed

Field Code Changed

357 cm scale crystals, reducing the need for small ablation volumes. While individual calcite crystals in other settings can  
358 sometimes be < 260 μm, the total amount of calcite is often large enough that aggregates of pure (or close to pure) calcite can  
359 be ablated. Caution should be used with such analysis however, as this may affect laser induced fractionation, individual  
360 crystals may be of different ages, and there may be micro inclusions of other minerals.

## 361 5.2 Advantages of in-situ Lu-Hf dating of calcite compared to other geochronological methods

362 The Previous dissolution-based Lu–Hf geochronology has produced scattered isochrons, indicative of isotopic disturbances  
363 (Maas et al., 2020). While individual data points are significantly less precise than dissolution based methods, the ability to  
364 gain spatially resolved data on a much smaller scale (>260 microns), as well as obtain a large number of analyses in a single  
365 session can make data interpretation easier. This is in contrast to the generally well constrained ages demonstrated in this study,  
366 highlighting one of the main advantages of the *in situ* approach: the ability to rapidly obtain high spatial resolution coupled  
367 with a much larger number of data points (Simpson et al., 2021a). Importantly, trace element data can be obtained simultaneously to interrogate each data point for  
368 inclusions or age zonation. Furthermore, calcite Lu–Hf dating can overcome two issues often encountered during U–Pb dating;  
369 (1) in contrast to Pb, calcite does not incorporate significant concentrations of common Hf, and; (2) Lu is comparatively  
370 resistant to thermal diffusion in calcite (Cherniak, 1998), increasing the likelihood of primary precipitation ages to be  
371 preserved. Although it should be acknowledged that fluid mobility and re-crystallisation of the calcite may affect Lu-Hf ages,  
372 and are difficult to predict. This opens the possibility that time constraints can be obtained for carbonates from the first three-  
373 quarters of Earth history that are generally difficult to date by other methods. Importantly, calcite is commonly associated with  
374 ore formation, meaning *in-situ* Lu–Hf dating affords the possibility to directly constrain the age of mineralising events and the  
375 temporal evolution of mineral deposit systems.

376  
377 From our work, we suggest samples ME1 and OL-MB calcite could be developed as primary reference materials due to being  
378 (1) common-Hf free, (2) homogenous in age across crystals up ~1cm cm in size, and (3) available in large quantities. We aim  
379 to characterize such reference materials and make them available to the wider geochronology community.

## 380 6 Conclusions and Future Directions

381 Calcite is among the most common of rock-forming minerals, meaning that *in-situ* Lu–Hf geochronology of calcite has  
382 enormous potential to constrain the age of formation and/or alteration of a range of igneous, sedimentary, metamorphic, and  
383 hydrothermal rock systems, including rock-types that are considered very difficult to date (e.g., marbles). This technique has  
384 particular application to mineral deposits as it allows for the ability to constrain the age of pre-ore, ore-stage and post-ore  
385 events (e.g., Fig. 3). Furthermore, given the successful dating of old (~2 Ga) calcite with <1 ppm Lu (e.g., sample P01; Table  
386 1), this technique has the potential to date old calcite from a variety of settings with relatively low HREE concentrations. *In-*  
387 *situ* Lu–Hf dating of calcite can be regarded as a complimentary, and in some cases alternative, technique to carbonate U–Pb  
388 dating, where Lu–Hf dating is well suited for older samples, or to obtain primary precipitation ages for systems affected by Pb

Field Code Changed

Field Code Changed

389 mobility. Coupling *in-situ* Lu–Hf dating with other isotopic systems (U–Th–Pb, C, O, Sr, Nd) may be particularly powerful for  
390 constraining the origin, nature and redox conditions of the fluids or melts from which the calcite precipitated.

391

#### 392 **Author contributions**

393

394 Author contributions: A Simpson (corresponding author): conceptualisation, method development, experimentation,  
395 manuscript drafting. S Glorie: conceptualisation, manuscript drafting, primary supervision. M Hand: conceptualisation,  
396 manuscript drafting, secondary supervision. C Spandler: Conceptualisation, sampling, manuscript drafting. S Gilbert: Method  
397 development, experimentation, manuscript drafting. B Cave. Experimentation, manuscript drafting.

398

#### 399 **Acknowledgments**

400 The authors would like to thank the MinEx CRC for funding this research. The initial method development and apatite dating  
401 were supported by the Australian Research Council DP200101881. [Dr Morgan Blades is thanked for supplying a sample of](#)  
402 [Otter Lake calcite](#). Dr Anthony Milnes from the Tate Museum at the University of Adelaide is acknowledged for help during  
403 sampling and Aoife McFadden is acknowledged for assistance in operating the SEM at Adelaide Microscopy. [Dr Nick Roberts](#)  
404 [and associate professor Donald Davis are thanked for constructive comments during review.](#)

405

#### 406 **References**

- 407 [Barfod, G. H., Krogstad, E. J., Frei, R., and Albarède, F., 2005, Lu–Hf and PbSL geochronology of apatites from Proterozoic terranes: A](#)  
408 [first look at Lu–Hf isotopic closure in metamorphic apatite: Geochimica et Cosmochimica Acta, v. 69, no. 7, p. 1847–1859.](#)
- 409 [Barker, S. L. L., Bennett, V. C., Cox, S. F., Norman, M. D., and Gagan, M. K., 2009, Sm–Nd, Sr, C and O isotope systematics in hydrothermal](#)  
410 [calcite–fluorite veins: Implications for fluid–rock reaction and geochronology: Chemical Geology, v. 268, no. 1–2, p. 58–66.](#)
- 411 [Basson, I., Lourens, P., Paetzold, H.-D., Thomas, S., Brazier, R., and Molabe, P., 2017, Structural analysis and 3D modelling of major](#)  
412 [mineralizing structures at the Phalaborwa copper deposit.: Ore Geology Reviews, v. 83, p. 30–42.](#)
- 413 [Breemen, O. v., and Corriveau, L., 2005, U–Pb age constraints on arenaceous and volcanic rocks of the Wakeham Group, eastern Grenville](#)  
414 [Province: Canadian Journal of Earth Sciences, v. 42, no. 10, p. 1677–1697.](#)
- 415 [Brugger, J., Liu, W., Etschmann, B., Mei, Y., Sherman, D. M., and Testemale, D., 2016, A review of the coordination chemistry of](#)  
416 [hydrothermal systems, or do coordination changes make ore deposits?: Chemical Geology, v. 447, p. 219–253.](#)
- 417 [Chew, D. M., Sylvester, P. J., and Tubrett, M. N., 2011, U–Pb and Th–Pb dating of apatite by LA-ICPMS: Chemical Geology, v. 280, no.](#)  
418 [1–2, p. 200–216.](#)
- 419 [Cosca, M. A., Essene, E. J., Mezger, K., and van der Pluijm, B. A., 1995, Constraints on the duration of tectonic processes: Protracted](#)  
420 [extension and deep-crustal rotation in the Grenville orogen: Geology, v. 23, no. 4, p. 361–364.](#)
- 421 [Debruyne, D., Hulsbosch, N., and Muchez, P., 2016, Unraveling rare earth element signatures in hydrothermal carbonate minerals using a](#)  
422 [source–sink system: Ore Geology Reviews, v. 72, p. 232–252.](#)
- 423 [Duncan, R. J., Stein, H. J., Evans, K. A., Hitzman, M. W., Nelson, E. P., and Kirwin, D. J., 2011, A New Geochronological Framework for](#)  
424 [Mineralization and Alteration in the Selwyn–Mount Dore Corridor, Eastern Fold Belt, Mount Isa Inlier, Australia: Genetic](#)  
425 [Implications for Iron Oxide Copper–Gold Deposits: Economic Geology, v. 106, no. 2, p. 169–192.](#)
- 426 [Elzinga, E. J., Reeder, R. J., Withers, S. H., Peale, R. E., Mason, R. A., Beck, K. M., and Hess, W. P., 2002, EXAFS study of rare-earth](#)  
427 [element coordination in calcite: Geochimica et Cosmochimica Acta, v. 66, no. 16, p. 2875–2885.](#)
- 428 [Fisher, C. M., and Vervoort, J. D., 2018, Using the magmatic record to constrain the growth of continental crust—The Eoarchean zircon Hf](#)  
429 [record of Greenland: Earth and Planetary Science Letters, v. 488, p. 79–91.](#)

Field Code Changed

430 Frei, R., Villa, I. M., Nagler, T. F., Kramers, J. D., Pryzbyłowicz, W. J., Prozesky, V. M., Hofman, B. A., and Kamber, B. S., 1997, Single  
431 mineral dating by the Pb-Pb step leaching method: assessing the mechanisms: *Geochimica et Cosmochimica Acta*, v. 61, no. 2, p.  
432 393-414.

433 Garrett, S. J., 1992, *The Geology and Geochemistry of the Mount Elliott Copper-Gold deposit, Northwest Queensland* [Masters thesis]:  
434 University of Tasmania, 139 p.

435 Gibson, H. L., Lafrance, B., Pehrsson, S., Dewolfe, M. Y., Gilmore, K., and Simard, R.-L., 2012, *The Volcanological and Structural*  
436 *Evolution of the Paleoproterozoic Flin Flon Mining District: Anatomy of a Giant VMS System*: Geoscience Canada.

437 Giles, D., and Nutman, A. P., 2002, SHRIMP U–Pb monazite dating of 1600–1580 Ma amphibolite facies metamorphism in the southeastern  
438 Mt Isa Block, Australia: *Australian Journal of Earth Sciences*, v. 49, no. 3, p. 455-465.

439 Glorie, S., Gillespie, J., Simpson, A., Gilbert, S., Khudoley, A., Priyatkina, N., Hand, M., and Kirkland, C. L., 2021, Detrital apatite Lu-Hf  
440 and U-Pb geochronology applied to the southwestern Siberian margin: in review.

441 Groves, D. I., and Vielreicher, N. M., 2001, The Phalaborwa (palabora) carbonatite-hosted magnetite-copper sulfide deposit, South Africa:  
442 an emd-member of the iron-oxide-copper-gold-rare earth element deposit group?: *Mineralium Deposita*, v. 36, p. 189-194.

443 Henrichs, I. A., O'Sullivan, G., Chew, D. M., Mark, C., Babechuk, M. G., McKenna, C., and Emo, R., 2018, The trace element and U-Pb  
444 systematics of metamorphic apatite: *Chemical Geology*, v. 483, p. 218-238.

445 Horstwood, M. S. A., Košler, J., Gehrels, G., Jackson, S. E., McLean, N. M., Paton, C., Pearson, N. J., Sircombe, K., Sylvester, P.,  
446 Vermeesch, P., Bowring, J. F., Condon, D. J., and Schoene, B., 2016, Community-Derived Standards for LA - ICP - MS U-(Th-  
447 )Pb Geochronology – Uncertainty Propagation, Age Interpretation and Data Reporting: *Geostandards and Geoanalytical Research*,  
448 v. 40, no. 3, p. 311-332.

449 Hu, Z., Gao, S., Liu, Y., Hu, S., Chen, H., and Yuan, H., 2008, Signal enhancement in laser ablation ICP-MS by addition of nitrogen in the  
450 central channel gas: *Journal of Analytical Atomic Spectrometry*, v. 23, no. 8.

451 Kennedy, A. K., Kamo, S. L., Nasdala, L., and Timms, N. E., 2011, GRENVILLE SKARN TITANITE: POTENTIAL REFERENCE  
452 MATERIAL FOR SIMS U-Th-Pb ANALYSIS: *The Canadian Mineralogist*, v. 48, no. 6, p. 1423-1443.

453 Koo, J., and Mossman, D. J., 1975, Origin and metamorphism of the Flin Flon stratabound Cu-Zn sulfide deposit, Saskatchewan and  
454 Manitoba: *Economic Geology*, v. 70, p. 48-62.

455 Kretz, R., Campbell, J. L., Hoffman, E. L., Hartree, R., and Teesdale, W. J., 1999, Approaches to equilibrium in the distribution of trace  
456 elements among the principal minerals in a high-grade metamorphic terrane: *Journal of Metamorphic Geology*, v. 8, p. 493-506.

457 Krogstad, R., and Walker, R. J., 1994, High closure temperatures of the U-Pb system in large apatites from the Tin Mountain pegmatite,  
458 Black Hills South Dakota, USA: *Geochemistry, Geophysics, Geosystems*, v. 58, p. 3845-3853.

459 Kroslovskaya, I., and Günther, D., 2007, Elemental fractionation in laser ablation-inductively coupled plasma-mass spectrometry: evidence  
460 for mass load induced matrix effects in the ICP during ablation of a silicate glass: *J. Anal. At. Spectrom.*, v. 22, no. 1, p. 51-62.

461 Lafrance, B., Gibson, H. L., Pehrsson, S., Schetselaar, E., Dewolfe, M. Y., and Lewis, D., 2016, Structural reconstruction of the Flin Flon  
462 volcanogenic massive sulfide mining district, Saskatchewan and Manitoba, Canada: *Economic Geology*, v. 111, p. 849-875.

463 Le Bras, L. Y., Bolhar, R., Bybee, G. M., Nex, P. A., Guy, B. M., Moyana, T., and Lourens, P., 2021, Platinum-group and trace elements in  
464 Cu-sulfides from the Loolekop pipe, Phalaborwa: implications for ore-forming processes: *Mineralium Deposita*, v. 56, p. 161-177.

465 Li, Q., Parrish, R. R., Horstwood, M. S. A., and McArthur, J. M., 2014, U–Pb dating of cements in Mesozoic ammonites: *Chemical Geology*,  
466 v. 376, p. 76-83.

467 Li, Y., and Vermeesch, P., 2021, Short communication: Inverse isochron regression for Re–Os, K–Ca and other chronometers:  
468 *Geochronology*, v. 3, no. 2, p. 415-420.

469 Maas, R., Apukhtina, O. B., Kamenetsky, V. S., Ehrig, K., Sprung, P., and Munker, C., 2020, Carbonates at the supergiant Olympe Dam  
470 Cu-U-Au-Ag deposit, South Australia part 2: Sm-Nd, Lu-Hf and Sr-Pb isotope constraints on the chronology of carbonate  
471 deposition: *Ore Geology Reviews*.

472 Marshall, L., 2003, *Brecciation within the Mary Kathleen Group of the Eastern Succession, Mt Isa Block, Australia: Implications of district-*  
473 *scale structural and metasomatic processes for Fe-oxide-Cu-Au mineralisation*. [PhD thesis]: James Cook University.

474 Migdisov, A., Williams-Jones, A. E., Brugger, J., and Caporuscio, F. A., 2016, Hydrothermal transport, deposition, and fractionation of the  
475 REE: Experimental data and thermodynamic calculations: *Chemical Geology*, v. 439, p. 13-42.

476 Nebel, O., Morel, M., and Vroon, P., 2009, Isotope Dilution Determinations of Lu, Hf, Zr, Ta and W and Hf Isotope Compositions of NIST  
477 SRM 610 and 612 Glass Wafers: *Geostandards and Geoanalytical Research*, v. 33, no. 4, p. 487-499.

478 Nie, F. J., Bjørlykke, A., and Nilsen, K. S., 1999, The Origin of the Proterozoic Bidjovagge Gold-Copper Deposit, Finnmark, Northern  
479 Norway, as Deduced from Rare Earth Element and Nd Isotopic Evidences on Calcites: *Resource Geology*, v. 49, no. 1, p. 13-25.

480 Norris, A., and Danyushevsky, L., 2018, *Towards estimating the complete uncertainty budget of quantified results measured by LA-ICP-MS*,  
481 *Goldschmidt*: Boston, USA.

482 Oliver, N., Butera, K., Rubenach, M., Marshall, L., Cleverley, J., Mark, G., Tullemans, F., and Esser, D., 2008, The protracted hydrothermal  
483 evolution of the Mount Isa Eastern Succession: A review and tectonic implications: *Precambrian Research*, v. 163, no. 1-2, p. 108-  
484 130.

485 Oliver, N. H., Cartwright, I., Wall, V. J., and Golding, S. D., 1993, The stable isotope signature of kilometre-scale fracturedominated  
486 metamorphic fluid pathways, Mary Kathleen, Australia: *Journal of Metamorphic Geology*, v. 11, no. 5, p. 705-720.

487 Oliver, N. H., Cleverley, J. S., Mark, G., Pollard, P. J., Fu, B., Marshall, L. J., Rubenach, M. J., Williams, P. J., and Baker, T., 2004, Modeling  
488 the Role of Sodic Alteration in the Genesis of Iron Oxide-Copper-Gold Deposits, Eastern Mount Isa Block, Australia *Economic*  
489 *Geology*, v. 99, no. 6, p. 1145-1176.

490 Page, R. W., and Sun, S. S., 1998, Aspects of geochronology and crustal evolution in the Eastern Fold Belt, Mt Isa Inlier: *Australian Journal*  
491 *of Earth Sciences*, v. 45, no. 3, p. 343-361.

492 Peng, J. T., Hu, R. Z., and Burnard, P. G., 2003, Samarium–neodymium isotope systematics of hydrothermal calcites from the Xikuangshan  
493 antimony deposit (Hunan, China): the potential of calcite as a geochronometer: *Chemical Geology*, v. 200, no. 1, p. 129-136.

494 Rasbury, E. T., and Cole, J. M., 2009, Directly dating geologic events: U-Pb dating of carbonates: *Reviews of Geophysics*, v. 47, no. 3.

495 Rayner, N. M., 2010, New U-Pb zircon ages from the Flin Flon Targeted Geoscience Initiative Project 2006-2009: Flin Flon and Hook Lake  
496 blocks: *Geological Survey of Canada, Current Research*, 2010-4, p. 1-12.

497 Ribeiro, B. V., Finch, M. A., Cawood, P. A., Faleiros, F. M., Murphy, T. D., Simpson, A., Glorie, S., Tedeschi, M., Armit, R., and Barrote,  
498 V. R., 2021, From microanalysis to supercontinents: insights from the Rio Apa Terrane into the Mesoproterozoic SW Amazonian  
499 Craton evolution during Rodinia assembly: *Journal of Metamorphic Geology*.

500 Ring, U., and Gerdes, A., 2016, Kinematics of the Alpenrhein-Bodensee graben system in the Central Alps: Oligocene/Miocene transtension  
501 due to formation of the Western Alps arc: *Tectonics*, v. 35, no. 6, p. 1367-1391.

502 Rivers, T., 2015, Tectonic Setting and Evolution of the Grenville Orogen: An Assessment of Progress Over the Last 40 Years: *Geoscience*  
503 *Canada*, v. 42, no. 1, p. 77-124.

504 Roberts, N. M. W., Drost, K., Horstwood, M. S. A., Condon, D. J., Chew, D., Drake, H., Milodowski, A. E., McLean, N. M., Smye, A. J.,  
505 Walker, R. J., Haslam, R., Hodson, K., Imber, J., Beaudoin, N., and Lee, J. K., 2020, Laser ablation inductively coupled plasma  
506 mass spectrometry (LA-ICP-MS) U-Pb carbonate geochronology: strategies, progress, and limitations: *Geochronology*, v. 2, no.  
507 1, p. 33-61.

508 Roberts, N. M. W., Rasbury, E. T., Parrish, R. R., Smith, C. J., Horstwood, M. S. A., and Condon, D. J., 2017, A calcite reference material  
509 for LA-ICP-MS U-Pb geochronology: *Geochemistry, Geophysics, Geosystems*, v. 18, no. 7, p. 2807-2814.

510 Roberts, N. M. W., and Walker, R. J., 2016, U-Pb geochronology of calcite-mineralized faults: Absolute timing of rift-related fault events  
511 on the northeast Atlantic margin: *Geology*, v. 44, no. 7, p. 531-534.

512 Schetselaar, E., Ames, D., and Grunsky, E., 2017, Integrated 3D Geological Modeling to Gain Insight in the Effects of Hydrothermal  
513 Alteration on Post-Ore Deformation Style and Strain Localization in the Flin Flon Volcanogenic Massive Sulfide Ore System:  
514 *Minerals*, v. 8, no. 1.

515 Schneider, D. A., Heizler, M. T., Bickford, M. E., Wortman, G. L., Condie, K. C., and Perilli, S., 2007, Timing constraints of orogeny to  
516 cratonization: Thermochronology of the Paleoproterozoic Trans-Hudson orogen, Manitoba and Saskatchewan, Canada:  
517 *Precambrian Research*, v. 153, no. 1-2, p. 65-95.

518 Schumann, D., Martin, R. F., Fuchs, S., and de Fourestier, J., 2019, Silicocarbonatitic melt inclusions in fluorapatite from the Yates prospect,  
519 Otter Lake, Québec: Evidence of marble anatexis in the central metasedimentary belt of the Grenville Province: *The Canadian*  
520 *Mineralogist*, v. 57, no. 5, p. 583-604.

521 Simpson, A., Gilbert, S., Tamblyn, R., Hand, M., Spandler, C., Gillespie, J., Nixon, A., and Glorie, S., 2021a, In-situ Lu Hf geochronology  
522 of garnet, apatite and xenotime by LA ICP MS/MS: *Chemical Geology*, v. 577.

523 Simpson, A., Glorie, S., Morley, C. K., Roberts, N. M. W., Gillespie, J., and Lee, J. K., 2021b, In-situ calcite U-Pb geochronology of  
524 hydrothermal veins in Thailand: New constraints on Indosinian and Cenozoic deformation: *Journal of Asian Earth Sciences*, v.  
525 206.

526 Söderlund, U., Patchett, P. J., Vervoort, J. D., and Isachsen, C. E., 2004, The  $^{176}\text{Lu}$  decay constant determined by Lu–Hf and U–Pb isotope  
527 systematics of Precambrian mafic intrusions: *Earth and Planetary Science Letters*, v. 219, no. 3-4, p. 311-324.

528 Spandler, C., Hammerli, J., Sha, P., Hilbert-Wolf, H., Hu, Y., Roberts, E., and Schmitz, M., 2016, MKED1: A new titanite standard for in  
529 situ analysis of Sm–Nd isotopes and U–Pb geochronology: *Chemical Geology*, v. 425, p. 110-126.

530 Staff, P. M., 1976, The Geology and the economic deposits of copper, iron, and vermiculite in the Palabora Igneous Complex, A brief  
531 review.: *Economic Geology*, v. 71, p. 177-192.

532 Stern, R. A., Syme, E. C., Bailes, A. H., and Lucas, S. B., 1995, Paleoproterozoic (1.90–1.86 Ga) arc volcanism in the Flin Flon Belt, Trans-  
533 Hudson Orogen, Canada: contributions to Mineralogy and Petrology, no. 119, p. 117–141.

534 Tamblyn, R., Hand, M., Simpson, A., Gilbert, S., Wade, B., and Glorie, S., 2021, In-situ laser ablation Lu–Hf geochronology of garnet  
535 across the Western Gneiss Region: Campaign-style dating of metamorphism: *Journal of the Geological Society*, p. jgs2021-2094.

536 Terakado, Y., and Masuda, A., 1988, The coprecipitation of rare-earth elements with calcite and aragonite: *Chemical Geology*, v. 69, no. 1,  
537 p. 103-110.

538 Vermeesch, P., 2018, IsoplotR: A free and open toolbox for geochronology: *Geoscience Frontiers*, v. 9, no. 5, p. 1479-1493.

539 Vervoort, J., 2014, Lu-Hf Dating: The Lu-Hf Isotope System, *Encyclopedia of Scientific Dating Methods*, p. 1-20.

540 Wang, S., and Williams, P. J., 2001, Geochemistry and origin of Proterozoic skarns at the Mount Elliott Cu-Au(-Co-Ni) deposit, Cloncurry  
541 district, NW Queensland, Australia: *Mineralium Deposita*, v. 36, p. 109-124.  
542 Whitehouse, M. J., and Russell, J., 1997, Isotope systematics of Precambrian marbles from the Lewisian complex of northwest Scotland:  
543 implications for Pb-Pb dating of metamorphosed carbonates: *Chemical Geology*, v. 136, no. 3-4, p. 295-307.  
544 Wu, F.-Y., Yang, Y.-H., Li, Q.-L., Mitchell, R. H., Dawson, J. B., Brandl, G., and Yuhara, M., 2011, In situ determination of U-Pb ages and  
545 Sr-Nd-Hf isotopic constraints on the petrogenesis of the Phalaborwa carbonatite Complex, South Africa: *Lithos*, v. 127, no. 1-2,  
546 p. 309-322.  
547 Xiang, D., Zhang, Z., Zack, T., Chew, D., Yang, Y., Wu, L., and Hogmalm, J., 2021, Apatite U-Pb Dating with Common Pb Correction  
548 Using LA-ICP-MS/MS: *Geostandards and Geoanalytical Research*, v. 45, no. 4, p. 621-642.  
549 Zhong, S., and Mucci, A., 1995, Partitioning of rare earth elements (REEs) between calcite and seawater solutions at 25°C and 1 atm, and  
550 high dissolved REE concentrations: *Geochimica et Cosmochimica Acta*, v. 59, no. 3, p. 443-453.  
551

552

553

554

555

556

557

558

559

560

561

562

563

564

565

566

567

568

569

570

571

572

573

574

575

576

577



578

579

580

581

582

583

584

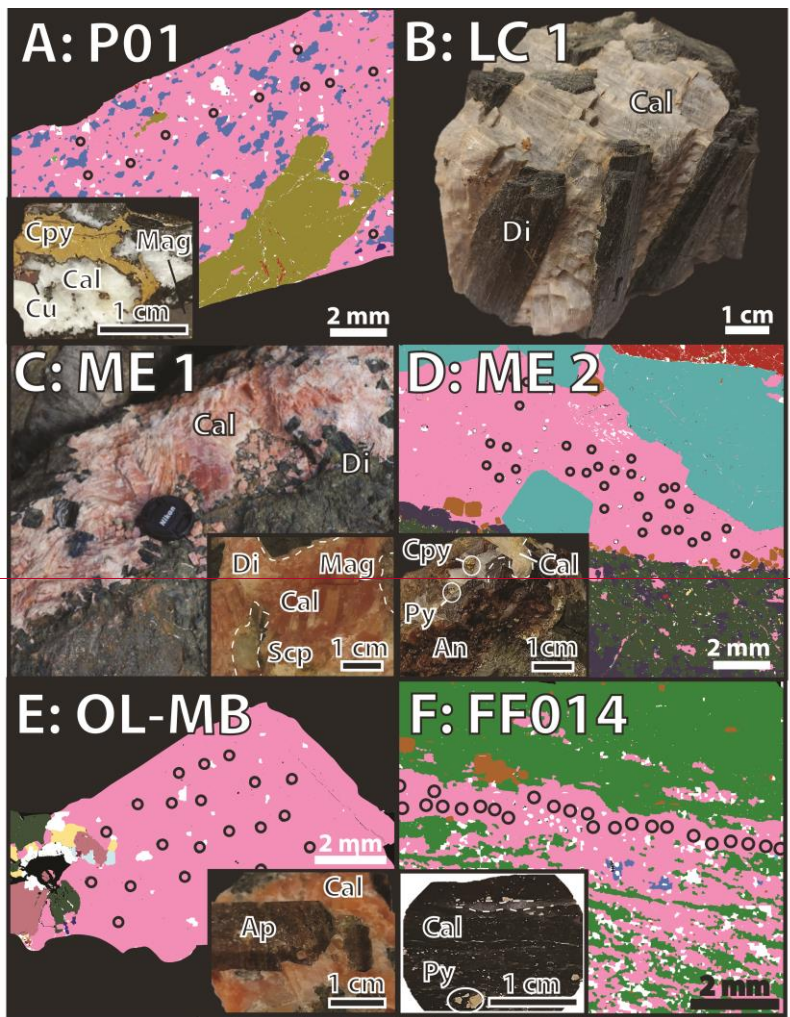
585

586

587

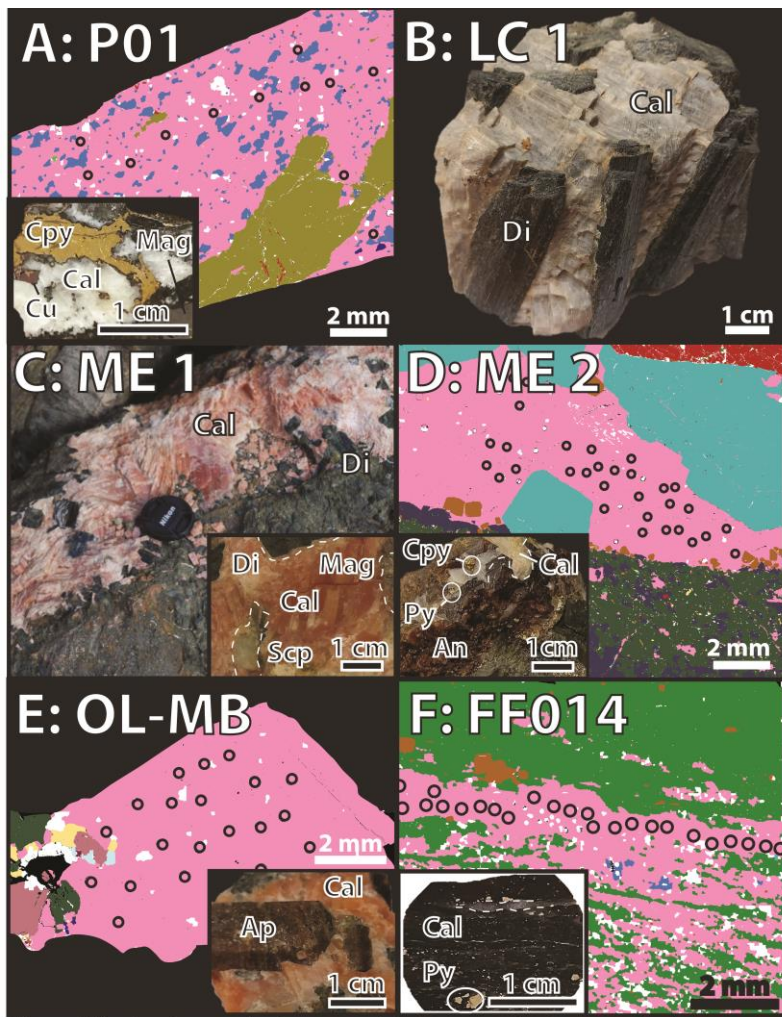
588

589 **Figures and Tables**



**Mineral Key**

<span style="display:inline-block; width:15px; height:15px; background-color: #FF69B4; border: 1px solid black;"></span> Calcite	<span style="display:inline-block; width:15px; height:15px; background-color: #4169E1; border: 1px solid black;"></span> Dolomite	<span style="display:inline-block; width:15px; height:15px; background-color: #40E0D0; border: 1px solid black;"></span> Andradite	<span style="display:inline-block; width:15px; height:15px; background-color: #3CB371; border: 1px solid black;"></span> Chlorite	<span style="display:inline-block; width:15px; height:15px; background-color: #FFD700; border: 1px solid black;"></span> Quartz
<span style="display:inline-block; width:15px; height:15px; background-color: #8B4513; border: 1px solid black;"></span> pyrite	<span style="display:inline-block; width:15px; height:15px; background-color: #808000; border: 1px solid black;"></span> Chalcopyrite	<span style="display:inline-block; width:15px; height:15px; background-color: #2E8B57; border: 1px solid black;"></span> Augite	<span style="display:inline-block; width:15px; height:15px; background-color: #DC143C; border: 1px solid black;"></span> Magnetite	<span style="display:inline-block; width:15px; height:15px; background-color: #C08080; border: 1px solid black;"></span> Microcline
<span style="display:inline-block; width:15px; height:15px; background-color: #ADD8E6; border: 1px solid black;"></span> Albite	<span style="display:inline-block; width:15px; height:15px; background-color: #483D8B; border: 1px solid black;"></span> Biotite	<span style="display:inline-block; width:15px; height:15px; background-color: #2F4F4F; border: 1px solid black;"></span> Aegirine/ Augite		

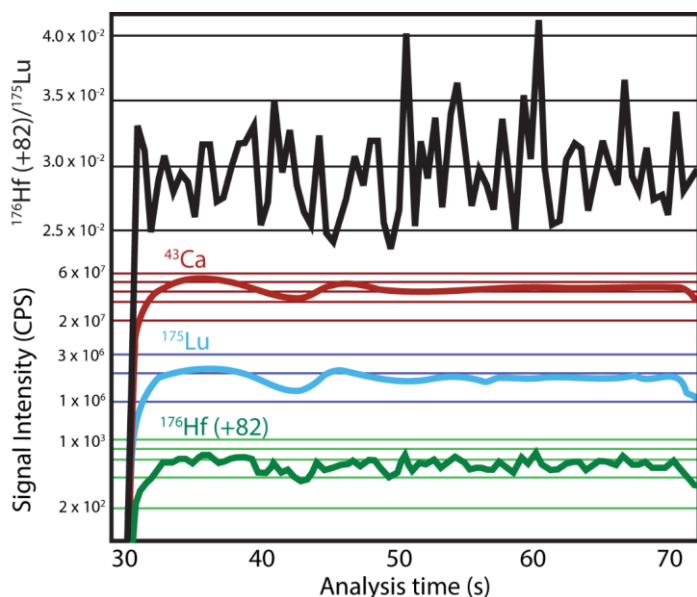


**Mineral Key**

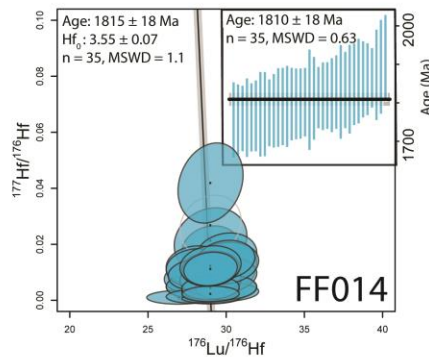
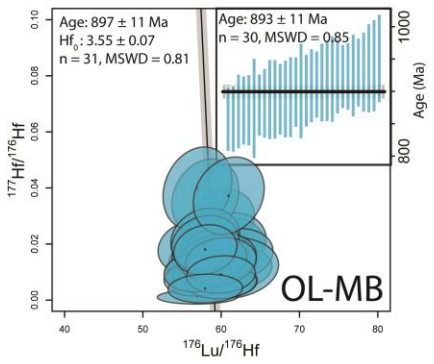
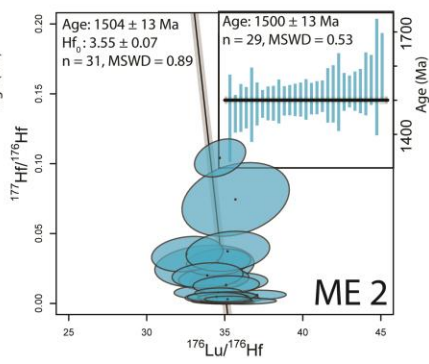
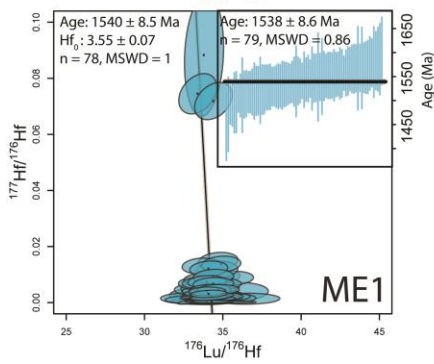
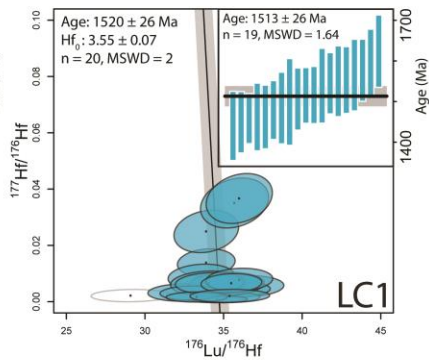
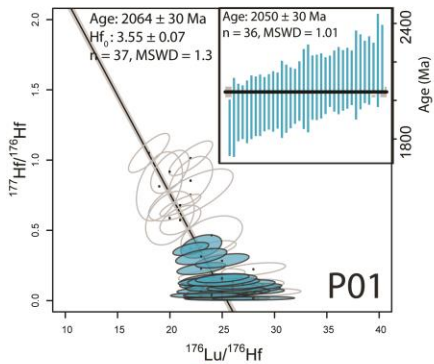
<span style="display: inline-block; width: 15px; height: 15px; background-color: #FF69B4; border: 1px solid black; margin-right: 5px;"></span> Calcite	<span style="display: inline-block; width: 15px; height: 15px; background-color: #4169E1; border: 1px solid black; margin-right: 5px;"></span> Dolomite	<span style="display: inline-block; width: 15px; height: 15px; background-color: #40E0D0; border: 1px solid black; margin-right: 5px;"></span> Andradite	<span style="display: inline-block; width: 15px; height: 15px; background-color: #228B22; border: 1px solid black; margin-right: 5px;"></span> Chlorite	<span style="display: inline-block; width: 15px; height: 15px; background-color: #FFD700; border: 1px solid black; margin-right: 5px;"></span> Quartz
<span style="display: inline-block; width: 15px; height: 15px; background-color: #8B4513; border: 1px solid black; margin-right: 5px;"></span> pyrite	<span style="display: inline-block; width: 15px; height: 15px; background-color: #808000; border: 1px solid black; margin-right: 5px;"></span> Chalcopyrite	<span style="display: inline-block; width: 15px; height: 15px; background-color: #2F4F4F; border: 1px solid black; margin-right: 5px;"></span> Augite	<span style="display: inline-block; width: 15px; height: 15px; background-color: #8B0000; border: 1px solid black; margin-right: 5px;"></span> Magnetite	<span style="display: inline-block; width: 15px; height: 15px; background-color: #483D8B; border: 1px solid black; margin-right: 5px;"></span> Aegirine/ Augite
<span style="display: inline-block; width: 15px; height: 15px; background-color: #483D8B; border: 1px solid black; margin-right: 5px;"></span> Biotite	<span style="display: inline-block; width: 15px; height: 15px; background-color: #C08080; border: 1px solid black; margin-right: 5px;"></span> Microcline	<span style="display: inline-block; width: 15px; height: 15px; background-color: #ADD8E6; border: 1px solid black; margin-right: 5px;"></span> Albite		

592 Figure 14: A combination of SEM mineral maps (A,C,D,E) and photos of analysed samples. (A) P01 (Phalaborwa Carbonatite) shows calcite in  
 593 petrogenetic context to chalcopyrite. (B) Photo of LC 1 hand sample. (C) Photo of the ME 1 sample in outcrop, with inset showing the mineralogy of  
 594 the analysed sample. (D) calcite from ME 2 (Mt Isa) in contact with hematite, pyrrhotite and andradite, with inset showing hand sample (D) OL-MB  
 595 (Otter Lake), showing analysed calcite with associated minerals, with inset showing relationship between apatite (Ap) and calcite (Cal) in hand  
 596 sample. (E) FF014 (Flin Flon deposit) shows calcite vein in chlorite matrix with disseminated pyrite, with inset showing analysed block (dark coloured  
 597 matrix is composed of chlorite). Black circles represent laser spot locations. Mineral abbreviations: Cal: Calcite, Cpy: chalcopyrite, Py: pyrite, Mag:  
 598 magnetite, Cu: cubanite, Di: diopside, Scp: scapolite, An: andradite. [Larger size sample images are included in appendix C.](#)

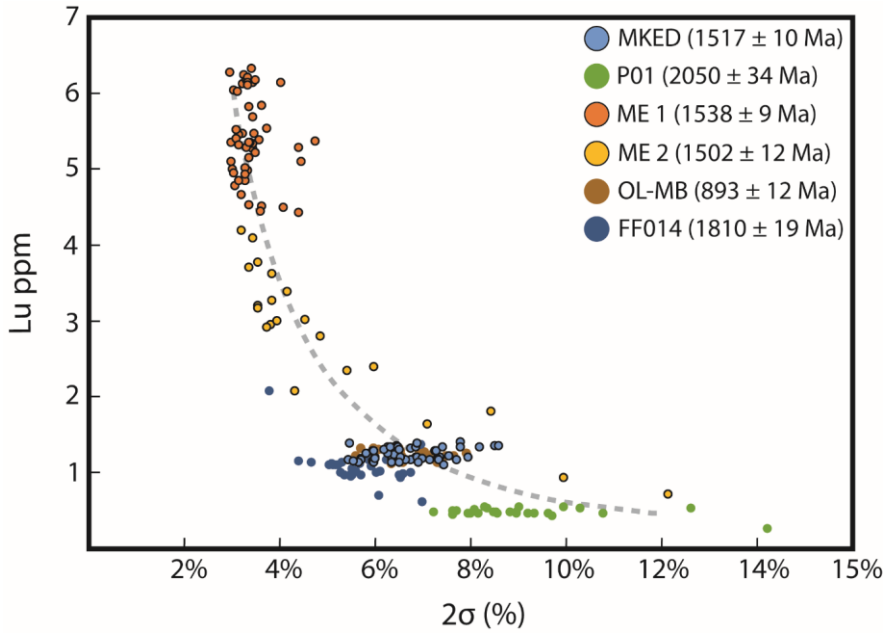
Field Code Changed



600  
 601 Figure 2: Time resolved signals for  $^{175}\text{Lu}(^{176})\text{Hf} (+82)$ ,  $^{43}\text{Ca}$ ,  $^{175}\text{Lu}$ , and  $(^{176})\text{Hf} (+82)$  demonstrating the effects of plasma loading on  
 602 the signal intensities (i.e. dip in signal intensities at ~10-15s ablation), but not for the  $^{176}\text{Hf}/^{175}\text{Lu}$  ratio isotope ratios, which remains constant down-  
 603 hole. The time resolved intensity of each analyte has been offset in the graph for better comparison, therefore the Y axis scale is not  
 604 continuous. Green horizontal lines show the scale for  $^{176}\text{Hf} (+82)$ , blue horizontal lines show the scale for  $^{175}\text{Lu}$ , red horizontal lines  
 605 show the scale for  $^{43}\text{Ca}$ , and black horizontal lines show the scale for the  $^{176}\text{Hf} (+82)/^{175}\text{Lu}$  ratio. Presented data is from an analysis  
 606 of MKED calcite.



608 Figure 3: Anchored inverse isochron and Wweighted average 'single spot' ages for analysed samples, corrected for matrix-induced  
 609 fractionation against MKED1 calcite. Isochrons have been anchored to an initial  $^{177}\text{Hf}/^{176}\text{Hf}$  ratio of  $3.55 \pm 0.07$ . Ellipses represent  
 610 data points and  $2\sigma$  uncertainty. Uncoloured ellipses represent data points excluded from the regression calculation. Weighted  
 611 average ages - are corrected and for common-Hf where relevant (see Table 1 and text). Blue bars represent  $2\sigma$  uncertainties. Black  
 612 lines represent weighted average ages, with grey boxes representing the 95% confidence interval uncertainty.



613  
 614 Figure 4: Lu ppm vs  $2\sigma$  uncertainty for each calcite analysis. The grey curve shows a function fitted to the data from samples with  
 615 ages between 1500 and 1540 Ma (samples ME1, ME2, and MKED, with symbols outlined in black). Only data points with similar  
 616 ages were used to construct this guiding curve as the obtained precision is age-dependant. The Lu-Hf ages for older samples (e.g.  
 617 P01 and FF014) are more precise relative to younger samples for a given Lu concentration (assuming no common Hf). Note: MKED  
 618 is the calcite Lu-Hf standard used to correct the analysed samples. All data for MKED is included in supplementary file 1.

619  
 620  
 621  
 622  
 623  
 624

625  
626  
627  
628

629 TABLE 1: AGES AND LU AND HF CONCENTRATION INFORMATION FOR THE ANALYSED SAMPLES.

<b>Sample</b>	<b>Age</b>	<b>95%</b>	<b>n</b>	<b>Min.</b>	<b>Av %</b>	<b>Max.</b>	<b>Min</b>	<b>Av</b>	<b>Max</b>	<b>Min</b>	<b>av Hf*</b>	<b>Max</b>
	<b>(Ma)</b>	<b>CI</b>		<b>% Hf</b>	<b>Hf</b>	<b>% Hf</b>	<b>Lu</b>	<b>Lu</b>	<b>Lu</b>	<b>Hf*</b>	<b>ppb</b>	<b>Hf</b>
				<b>corr</b>	<b>corr</b>	<b>corr</b>	<b>ppm</b>	<b>ppb</b>	<b>ppb</b>	<b>ppb</b>		<b>ppb</b>
<b>P01</b>	2054	1.54%	36	0%	2.65%	13%	270	505	557	0.03	0.270	1.00
<b>LC 1</b>	1513	1.7%	19	0.16%	0.46%	1.25%	1900	1600	3600	0.011	0.090	0.360
<b>ME 1</b>	1540	0.65%	79	0%	0.28%	2.4%	4300	5325	6300	0.002	0.150	1.80
<b>ME 2</b>	1500	0.98%	29	0.16%	0.58%	3.04%	700	3159	5500	0.002	0.110	0.340
<b>OL-MB</b>	892	1.42%	30	0.16%	0.58%	1.25%	1100	1200	1300	0.003	0.050	0.120
<b>FF014</b>	1807	1.00-9%	35	0.16%	0.39%	1.3%	616	1020	1170	0.004	0.052	0.210

630 *Note: 95% CI refers to the 95% confidence interval uncertainty on the calculated age. n refers to the number of analyses used for the*  
 631 *age calculation. % Hf corr refers to the average % decrease in age due to the common Hf correction. Hf\* concentrations have been*  
 632 *calculated from <sup>178</sup>Hf and assume no radiogenic ingrowth of <sup>176</sup>Hf and thus represent the 'common' Hf concentration for each sample.*

633

634 **Appendix A: MKED calcite sample description**

635 A sample of orange-pink calcite associated with the MKED1 titanite U-Pb standard (1517.32 ± 0.32 Ma, U-Pb TIMS; Spandler  
 636 et al., 2016) was analysed as a matrix matched secondary standard in order to correct unknown samples for matrix related  
 637 analytical offsets, such as laser induced elemental fractionation and plasma loading effects. The calcite was sampled from the  
 638 same drill core from which the titanite standard was taken (full details can be found in Spandler et al., 2016). The sample  
 639 consists of massive calcite surrounding large (~8Xcm) euhedral titanite crystals. The titanite is interpreted to have grown in  
 640 the same fluid as the calcite, but just prior to calcite crystallization. The average age across all 4 analytic sessions is 1560 ± 10  
 641 Ma (fig. A2), suggesting that matrix fractionation during laser ablation produces ages that are systematically approximately  
 642 3% too old

Formatted: Font color: Auto

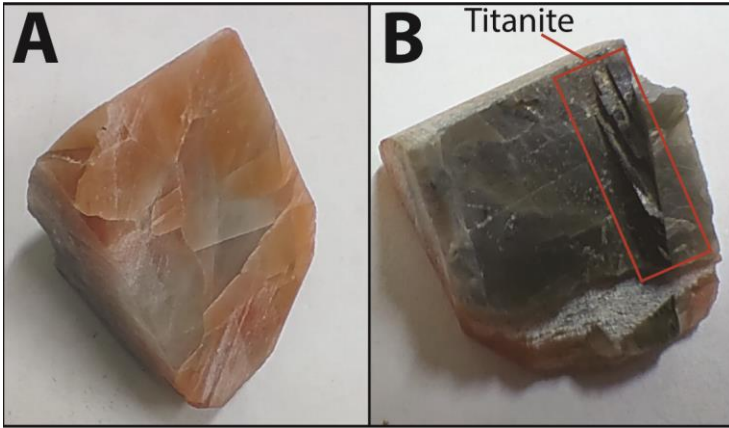
Formatted: Font color: Auto

Formatted: Font color: Auto

Formatted: Font color: Auto

Formatted: Font color: Auto

Formatted: Font color: Auto



643

644 **Figure A1:** images of MKED calcite. A shows calcite chip from where the analysed sample was taken. B shows underside of the same

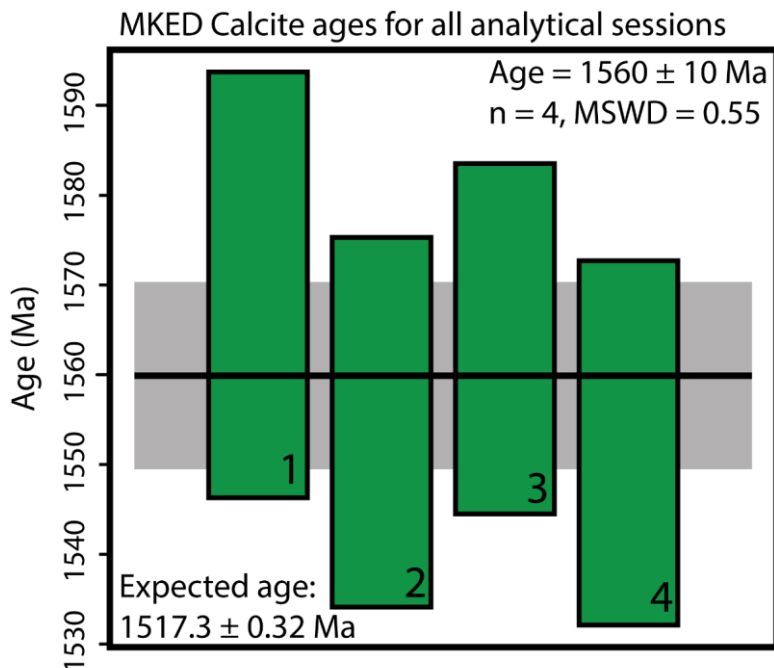
645 chip, where a large titanite crystal has been removed. Red box shows remnant fragments of titanite.

646

Formatted: Caption, Line spacing: Double



647 **Supplementary figure 1:** images of MKED calcite. A shows calcite chip from where the analysed sample was taken. B shows



Formatted: Font color: Auto

Formatted: Font color: Auto

Formatted: Font color: Auto

648 **Figure A2:** Demonstration of the systematic analytical offset observed for calcite Lu-Hf ages. Green rectangles are 95% confidence

649 intervals around weighted mean ages for each session, with session number in the bottom right corner of each rectangle. Horizontal

650 black line shows the weighted average age of all analytical sessions, with grey rectangle showing 95% confidence interval uncertainty.

651 The combined weighted average age for all analytical sessions is shown in the top right corner. The expected age is from Spandler

652 et al. (2016). Weighted mean ages were calculated using ISOPLOTR (Vermeesch, 2018).

653

654

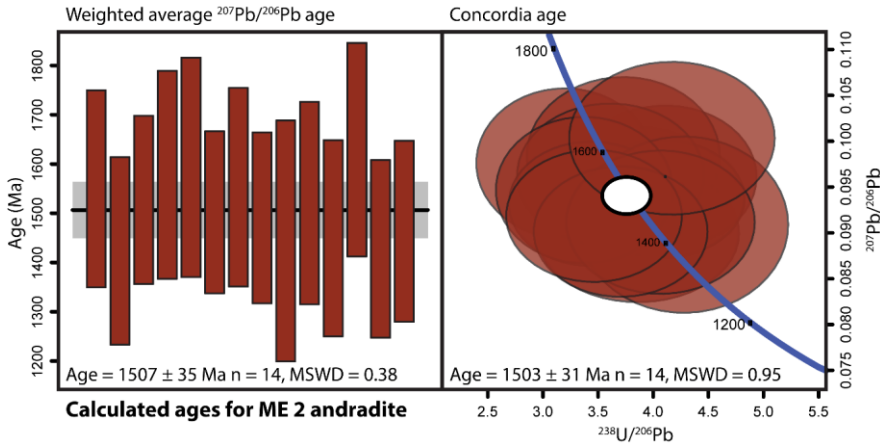
655

656 Cogenetic andradite was analysed from the Mt Elliott 2 calcite sample (fig. 1). The sample was analysed using the same laser

657 system as used for Lu-Hf analysis, but coupled with an Agilent 7900 quadrupole mass spectrometer. As the University of

658 Adelaide does not currently possess an andradite U-Pb standard, U-Pb and Pb-Pb ratios were corrected to NIST610 SRM,

659 using ratios from (REF). A large aspect ratio ablation spot (120 microns in diameter, drilling approximately 30 microns deep)  
 660 was used to minimise the effects of downhole fractionation (REF – Sylvester?) however, it is possible that calculate U-Pb ages  
 661 are inaccurate due to the lack of matrix matched primary standard. As the data appears to be concordant, however, a weighted  
 662 average age can be calculated from the  $^{207}\text{Pb}/^{206}\text{Pb}$  ratios (fig. B1X), which should not be significantly affected by laser induced  
 663 matrix fractionation (REF). As such, the calculated age is considered accurate within uncertainty.

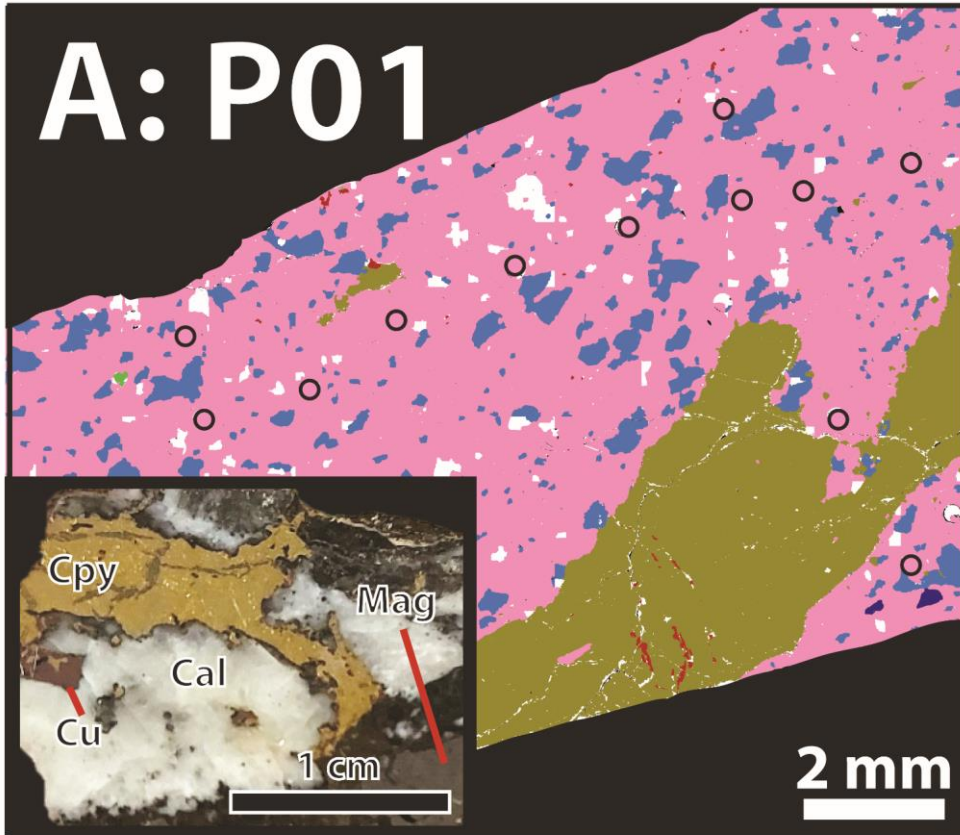


664 Figure B1: U-Pb age of ME 2 andradite. Left panel shows the weighted average  $^{207}\text{Pb}/^{206}\text{Pb}$  age and the right panel shows the  
 665 concordia age on a Tera-Wasserburg Concordia plot. For the weighted average, vertical rectangles are  $2\sigma$  uncertainties around  
 666 calculated single spot ages, with the black bar showing calculated weighted mean age, and the grey rectangle showing associated  
 667 95% confidence interval uncertainty. For the concordia plot, each ellipse shows the  $2\sigma$  uncertainty around each analysis, with white  
 668 ellipse representing 95% confidence interval uncertainty around the calculated concordia age. Weighted mean age and concordia  
 669 age were calculated using ISOPLOTR (Vermeesch, P., 2018).

671 Appendix C: Large sample images

672 The following are larger versions of the sample images from figure 1. Mineral abbreviations are: Cal: Calcite, Cpy:  
 673 chalcopryite, Py: pyrite, Mag: magnetite, Cu: cubanite, Di: diopside, Scp: scapolite, An: andradite

674

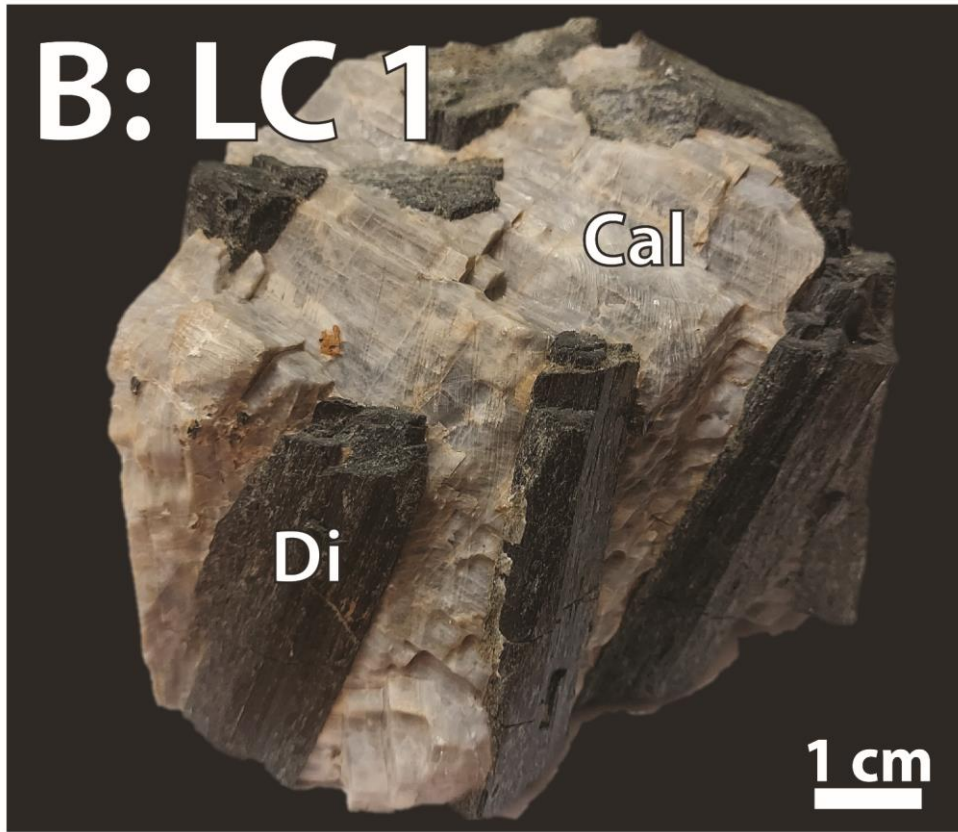


Calcite
  Dolomite
  Chalcopyrite
  Magnetite

675  
 676 Figure C1: Large image of sample P01 from Phalaborwa carbonatite, South Africa. Large images shows SEM mineral map. Inset  
 677 shows hand sample photo. Cpy: Chalcopyrite, Cu: Cubanite, Cal: calcite, Mag: Magnetite.

678 age is considered to be accurate within uncertainty of its U-Pb age.

679

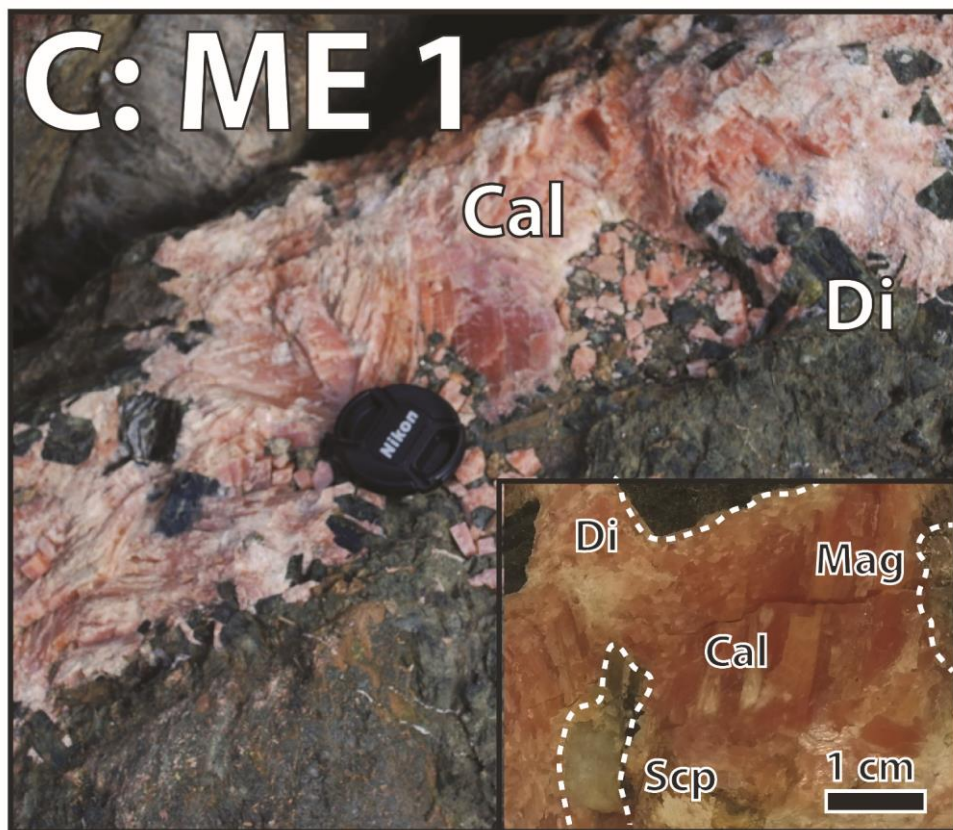


680

681 Figure C2: Large image of sample LC1 from Lime Creek, Mt Isa region, Australia. Image shows hand sample. Di: diopside, Cal:

682 calcite.

683

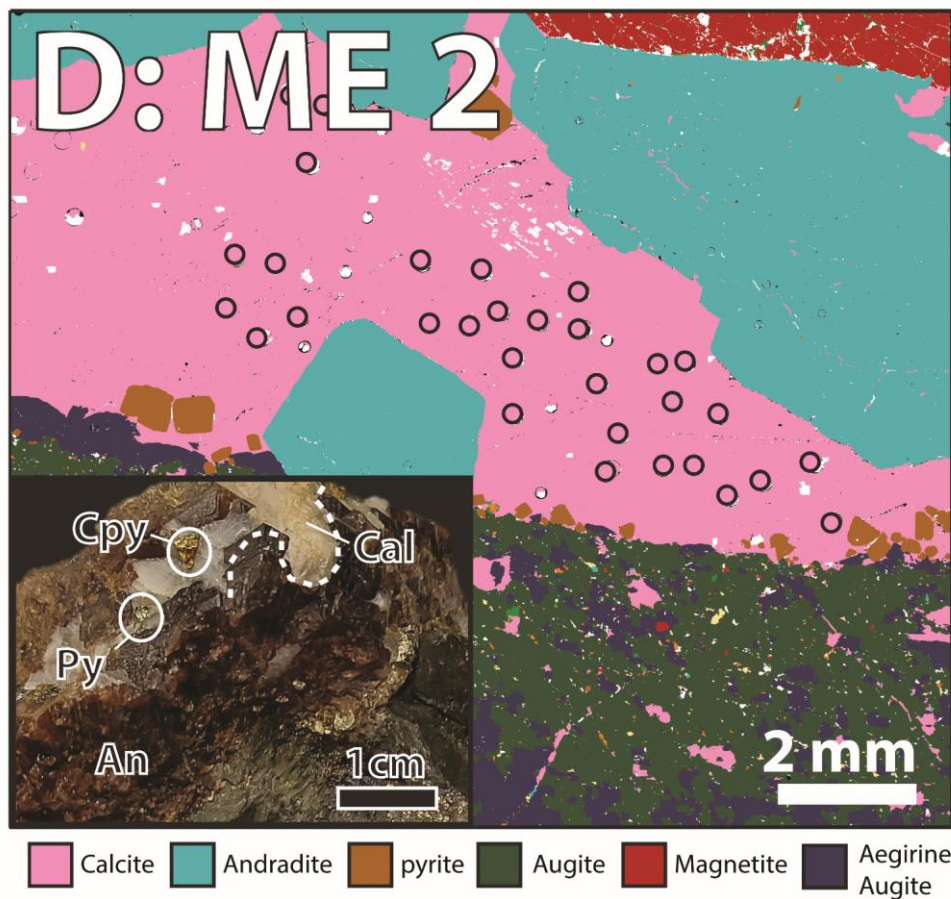


684

685 Figure C3: Large image of sample ME1 from Mt Elliott, Mt Isa region, Australia. Large images shows sample location and inset

686 shows hand sample. Di: diopside, Scp: scapolite, Cal: calcite, Mag: magnetite

687



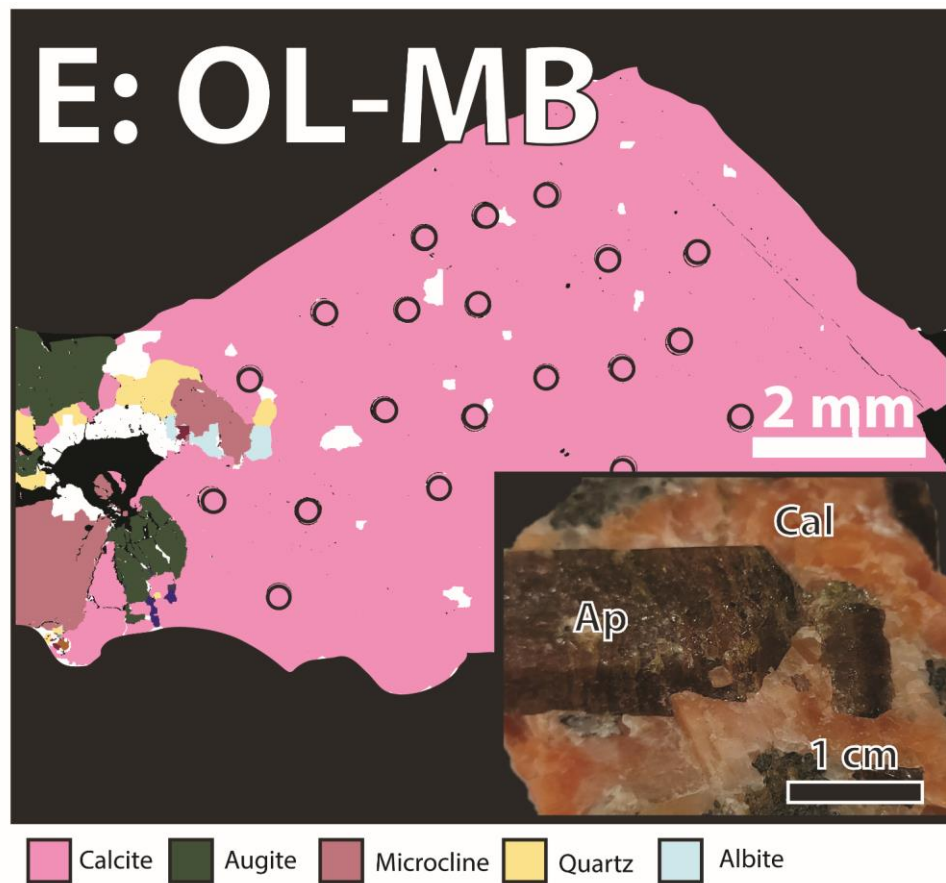
688

689

690

691

**Figure C4: Large image of sample ME2 from Mt Elliott, Mt Isa region, Australia. Large images shows SEM mineral map with black circles showing laser spot locations. Inset shows hand sample photo. Cpy: Chalcopyrite, Py: pyrite, Cal: calcite, An: andradite.**

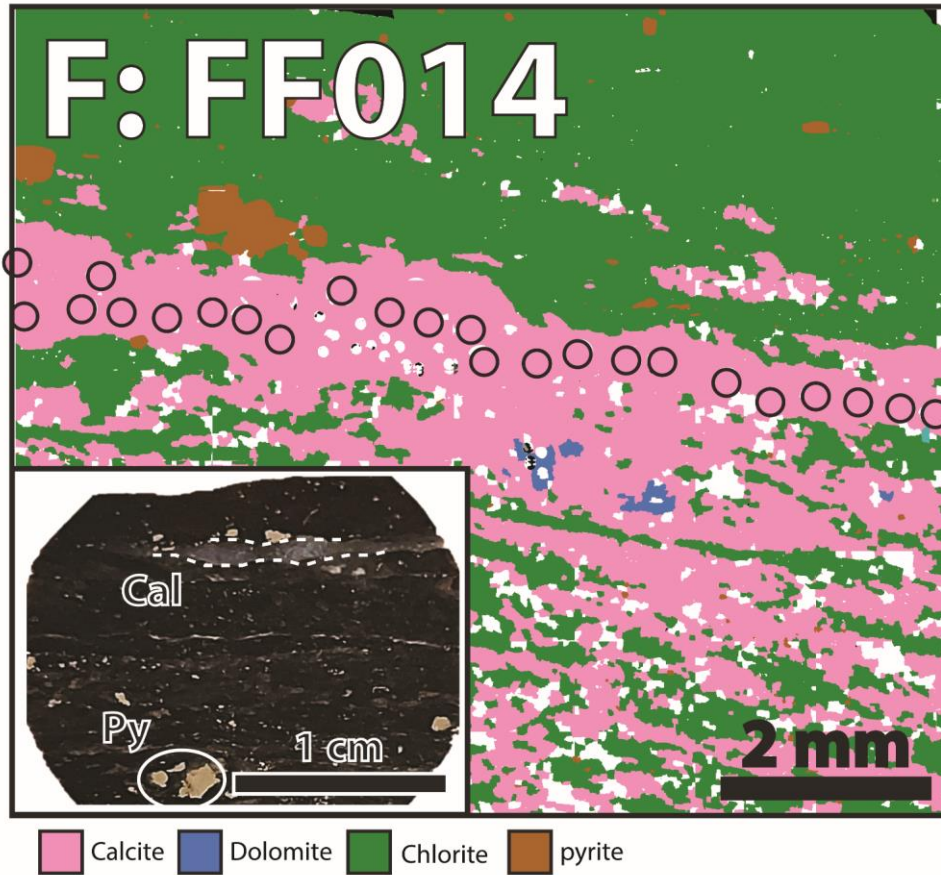


692

693 Figure C5: Large image of sample OL-MB from the Yates mine, Canada. Large images shows SEM mineral map with black circles

694 showing laser spot locations. Inset shows hand sample photo. Ap: apatite, Cal: calcite.

695



696

697 Figure C6: Large image of sample FF014 from Flin Flon, Manitoba and Saskatchewan, Canada. Large images shows SEM mineral

698 map with black circles showing laser spot locations. Inset shows hand sample photo. Py: pyrite, Cal: calcite.

699

700

701

702



703  
704  
705  
706

**APPENDIX TABLE 1: ANALYSIS AND LA-ICP-MS/MS TUNING PARAMETERS**

**plasma parameters**

<u>RF power</u>	<u>1350 W</u>
<u>Sample Depth</u>	<u>4 mm</u>
<u>Ar carrier gas</u>	<u>0.94 L/min</u>
<u>He carrier gas</u>	<u>0.38 L/min</u>
<u>N<sub>2</sub> addition</u>	<u>3.5 mL/min</u>

**Lens Parameters**

<u>Extract 1</u>	<u>-1.5 V</u>
<u>Extract 2</u>	<u>-140 V</u>
<u>Omega Bias</u>	<u>-70 V</u>
<u>Omega Lens</u>	<u>8.0 V</u>
<u>Q1 entrance</u>	<u>-45 V</u>
<u>Q1 exit</u>	<u>1.0 V</u>
<u>Cell focus</u>	<u>1.0 V</u>
<u>Cell Entrance</u>	<u>-120 V</u>
<u>Cell Exit</u>	<u>-100 V</u>
<u>Deflect</u>	<u>10.0 V</u>
<u>Plate Bias</u>	<u>-60 V</u>

**Q1 parameters**

<u>Q1 bias</u>	<u>-1.0 V</u>
<u>Q1 Prefilter Bias</u>	<u>-10.0 V</u>
<u>Q1 Postfilter Bias</u>	<u>-10.0 V</u>
<b><u>Cell Parameters</u></b>	
<u>He flow</u>	<u>1.0 mL/min</u>
<u>10% HN<sub>3</sub> + 90% He gas</u>	<u>3 mL/min</u>
<u>flow</u>	
<u>Octopole bias</u>	<u>-2.0 V</u>
<u>Axial Acceleration</u>	<u>2.0 V</u>
<u>Octopole RF</u>	<u>180 V</u>
<u>Energy Discrimination</u>	<u>-13.0 V</u>
<b><u>Q2 parameters</u></b>	
<u>Q2 bias</u>	<u>-15 V</u>
<u>Wait time offset</u>	<u>5ms</u>
<b><u>Analysis Parameters</u></b>	
<u>Laser wavelength</u>	<u>193 nm</u>
<u>Laser fluence</u>	<u>10 J/cm<sup>2</sup></u>
<u>Laser spot diameter</u>	<u>257 μm (43 μm; NIST610 glass)</u>
<u>Laser repetition rate</u>	<u>10 Hz</u>
<u>washout</u>	<u>30 s (post cleaning pulse) + 20 s (post analysis)</u>
<u>Background</u>	<u>30 s</u>
<u>Analysis time</u>	<u>40 s</u>

<i>Isotopes measured/dwell</i>	$^{27}\text{Al}$ (2), $^{43}\text{Ca}$ (2), $^{47}\text{Ti}$ (2), $^{89}\text{Y}$ (2), $^{90}\text{Zr}$ (2), $^{140}\text{Ce}$ (2), $^{172}\text{Yb}$
<i>times (ms)</i>	(10), $^{175}\text{Lu}$ (10), $^{175+82}\text{Lu}$ (100), $^{176+82}\text{Hf}$ (150), $^{178+82}\text{Hf}$ (150)

707

708

**Formatted:** Font: 10 pt, Not Bold